Elsevier Editorial System(tm) for Computers and Geotechnics

Manuscript Draft

Manuscript Number: COGE-D-15-00438R2

Title: DEM modelling of cone penetration test in a double-porosity crushable granular material

Article Type: Research Paper

Keywords: Discrete element method, pumice sand, cone penetration, particle crushing, double porosity

Corresponding Author: Dr. Matteo Oryem Ciantia, Ph.D.

Corresponding Author's Institution: Universitat Politècnica de Catalunya

First Author: Matteo Oryem Ciantia, Ph.D.

Order of Authors: Matteo Oryem Ciantia, Ph.D.; Marcos Arroyo; Joanna Butlanska ; Antonio Gens

Abstract: A three-dimensional discrete element model is used to investigate the effect of grain crushing on the tip resistance measured by cone penetration tests (CPT) in calibration chambers. To do that a discrete analogue of pumice sand, a very crushable microporous granular material, is created. The particles of the discrete model are endowed with size-dependent internal porosity and crushing resistance. A simplified Hertz-Mindlin elasto-frictional model is used for contact interaction. The model has 6 material parameters that are calibrated using one oedometer test and analogies with similar geomaterials. The calibration is validated reproducing other element tests. To fill a calibration chamber capable of containing a realistic sized CPT the discrete analogue is up-scaled by a factor of 25. CPT is then performed at two different densities and three different confinement pressures. Cone tip resistance in the crushable material is practically insensitive to initial density, as had been observed in previous physical experiments. The same CPT series is repeated but now particle crushing is disabled. The ratios of cone tip resistance between the two types of simulation are in good agreement with previous experimental comparisons of hard and crushable soils. Microscale exploration of the models indicates that crushing disrupts the buttressing effect of chamber walls on the cone.

DEM modelling of cone penetration tests in a double-porosity crushable granular material

Matteo Oryem Ciantia, Marcos Arroyo, Joanna Butlanska & Antonio Gens

Departamiento de Ingeniería del Terreno, UPC, Barcelona, Spain, - matteo.ciantia@upc.edu

ABSTRACT

A three-dimensional discrete element model is used to investigate the effect of grain crushing on the tip resistance measured by cone penetration tests (CPT) in calibration chambers. To do that a discrete analogue of pumice sand, a very crushable microporous granular material, is created. The particles of the discrete model are endowed with size-dependent internal porosity and crushing resistance. A simplified Hertz-Mindlin elasto-frictional model is used for contact interaction. The model has 6 material parameters that are calibrated using one oedometer test and analogies with similar geomaterials. The calibration is validated reproducing other element tests. To fill a calibration chamber capable of containing a realistic sized CPT the discrete analogue is up-scaled by a factor of 25. CPT is then performed at two different densities and three different confinement pressures. Cone tip resistance in the crushable material is practically insensitive to initial density, as had been observed in previous physical experiments. The same CPT series is repeated but now particle crushing is disabled. The ratios of cone tip resistance between the two types of simulation are in good agreement with previous experimental comparisons of hard and crushable soils. Microscale exploration of the models indicates that crushing disrupts the buttressing effect of chamber walls on the cone.

KEY WORDS:

Discrete element method, pumice sand, cone penetration, particle crushing, double porosity

1. Introduction:

Cone penetration tests (CPT) are extensively used for the site investigation of granular soils. The most common approach (Lunne et al. 1997; Schnaid, 2009; Robertson, 2009) to estimate strength, stiffness and other engineering properties of granular soils using CPT is to first infer soil state variables (e.g. relative density) from the measured CPT cone tip resistance. These inferences are typically supported by correlations established in calibration chambers; the most extensive databases are those established for silicate sands, such as Ticino (Jamiolkowski et al. 2003). Various micromechanical factors are known to have an influence on the observed CPT response in calibration chambers: one of the most important is grain strength or crushability.

Crushable sands are often formed by grains that are themselves porous. This makes them double porosity materials, i.e. materials which are porous at two separate scales of observation. Almeida et al. (1991) observed that cone resistance increased faster with initial relative soil density in silica sand (Ticino) than in calcareous Quiou sand. This was also observed by Wesley (2007) on volcanic pumice sand. Indeed, his results included an extreme case of that phenomenon: cone tip resistance measured in the calibration chamber appeared completely insensitive to initial relative density (Figure 1 illustrates the case for vertical confining pressure, σ_v of 200 kPa).

If strong-sand based correlations are used to interpret CPT results on more fragile soils relative density and frictional strength will be underestimated. This has large implications for CPT-based quality control procedures of soil treatments (Wehr, 2005). Particle crushing induced during CPT is also problematic when CPT-based field estimates of liquefaction are compared with laboratory tests (Moss, 2014) or when correlating CPT with other in situ test results, such as the SPT (Ahmed et al. 2014).

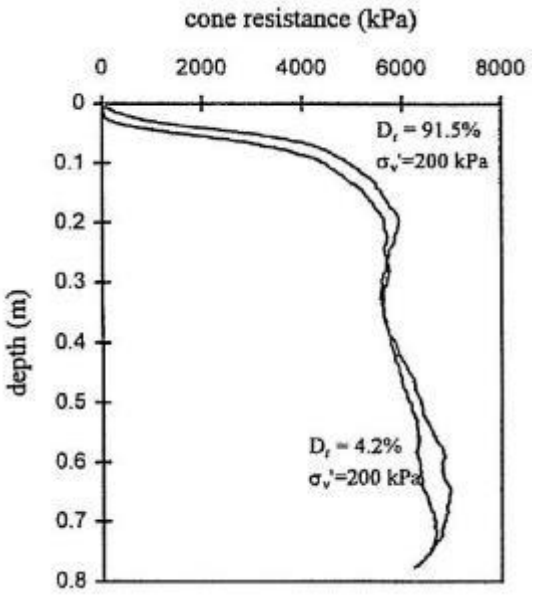

Figure 1 Calibration chamber CPT results on pumice sand as reported by Wesley (2007). Depth is measured with respect to the top of the calibration chamber

Addressing this problem only by means of extended empirical observations is possible, but slow and costly. Furthermore, it is also difficult to experimentally isolate the effects of grain strength; sands of different crushability might also differ in grain size, grain shape, etc. It is then desirable to complement and extend the relevant databases using numerical models that can represent and isolate the effect of grain crushability. Several approaches based on suitably formulated continuum models are possible (Zhang et al. 2013; Meier & Wehr, 2014). Another possibility is to use the discrete element method, which is well adapted both to incorporate micro-scale information and to represent problems involving large displacements such as the CPT (Lobo-Guerrero & Vallejo, 2005; Arroyo et al. 2011; McDowell et al. 2012; Quezada et al. 2014; Butlanska et al. 2014a).

The authors have recently proposed and tested a crushable soil DEM modelling approach that showed good ability to reproduce macroscopic responses of a variety of soils, (Ciantia et al. 2014a, 2015). The model was later extended to include double porosity granular materials (Ciantia et al. 2014b). The extended model is here applied to create a discrete analogue for the volcanic pumice sand tested by Wesley (2007).

In what follows we describe first the modelling approach employed to represent crushing in DEM models. Particular detail is given to describe how internal particle porosity is taken

71 into account. Calibration and validation of the model with laboratory specimen tests is then
72 presented. Finally a calibration chamber (CC) model is built in which a series of CPT
73 analogous to those reported in Wesley (2007) are performed. Test results are mostly examined
74 in terms of observed macroscopic responses, although some particle-scale results are also
75 discussed. All the numerical models described here were built using the PFC3D code (Itasca,
76 2010).
77

2. A crushable DEM model

Grain crushing may be modeled using the discrete element method (DEM) via two alternative methods: (1) replacing broken elements with new, smaller ones or (2) by using breakable element agglomerates. The latter is helpful for a detailed understanding of the micromechanics of grain failure (Cheng et al. 2003; Bolton et. al. 2008; Zhao 2013; Zhao et al. 2015). The former is more practical for the modeling of larger scale problems as shown by several examples in 2D (Lobo-Guerrero & Vallejo, 2005; Ben-Nun & Einav, 2010) and 3D (Bruchmüller et al. 2011; Esnault & Roux, 2013). The approach followed here is that of single grain replacement.

2.1 Particle failure

The failure criteria used in the model was inspired by Russell & Wood (2009) and Russell et al. (2009). These authors combined a two-parameter material strength criterion with the analysis of the elastic stress distribution induced by point loads on a sphere to obtain a practical failure criterion. Without entering into the details of the mathematical formulation, the final result of their analysis can be summarized as follows: independent of the particle coordination number, a particle subjected to a set of external point forces will reach failure when the maximum force (F) acting on it reaches a limit condition:

$$F \le \sigma_{\lim} \pi r^2 \sin^2 \theta_0 = \sigma_{\lim} A_F \tag{1}$$

where σ_{lim} is the limit strength of the material, r is the particle radius and θ_0 is half of the solid angle "seen" from the center of the particle which defines the small area of stress application, A_F (Figure 2). As indicated in Eq. (1) the limiting force is obtained as the product of a limit strength value, σ_{lim}, dependent on material parameters, and a contact area A_F.

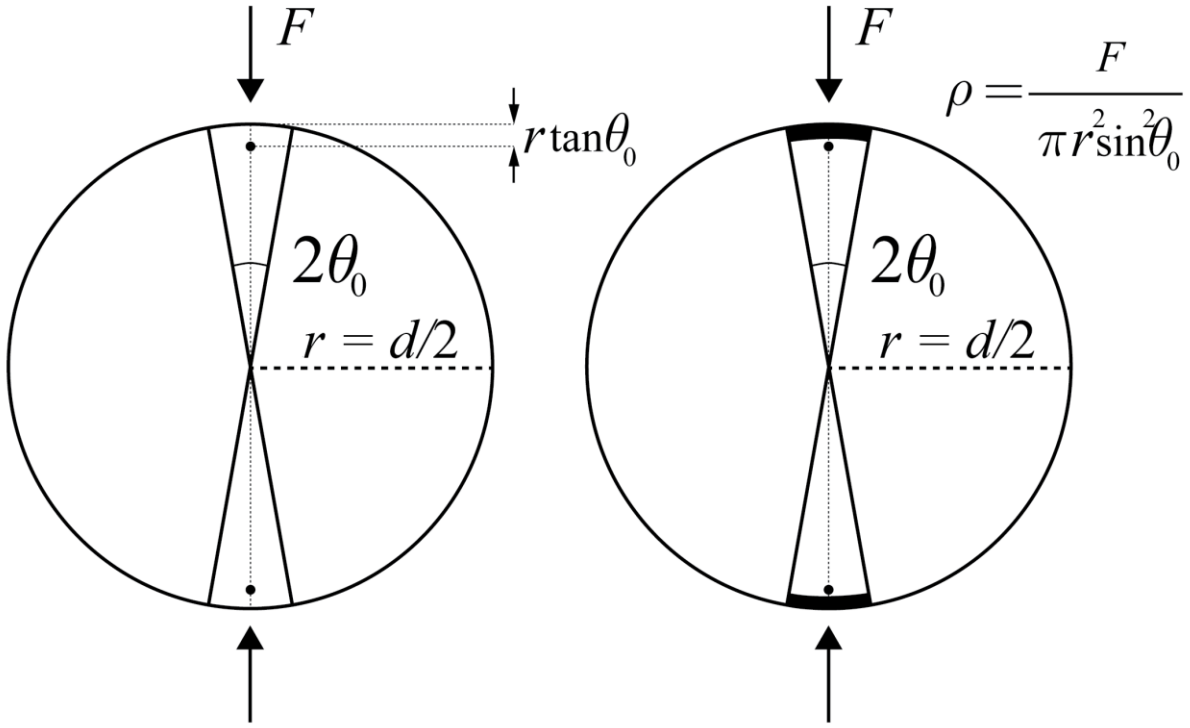

Figure 2 A point force *F* applied on a particle is distributed on an area subtended by angle θ_0.

There is a large natural variability in shape, composition, microstructure and contact conditions in soils. This variability is observed, for instance, in single grain crushing experiments, both as dispersion of force measurements for particles having the same nominal size, and as a size dependency of the average strength values. To incorporate that variability into the model, the limit strength, σ_{lim}, is assumed to be normally distributed for a given sphere size. This effect is incorporated as a dependency of the mean strength value through a correction factor, f_1. The coefficient of variation of the distribution (*var)* is design as a material parameter.

It has been repeatedly observed in single-particle crushing experiments that smaller particles are stronger than larger ones. This size effect in particle strength is incorporated as a dependency of the mean strength value on particle diameter through a second correction factor, f_2. This correction factor is casted in a Weibull-like form, Eq. (2). However, the Weibullian statistics for strength (Weibull, 1951) are not assumed, and *m* and *var* are independent parameters (Jansen & Stoyan, 2000; Brzesowsky et al, 2011). Following McDowell & Bono (2013), Eq. (2) may be simply described as a hardening rule.

$$\sigma_{\lim} = \sigma_{\lim,0} f_1(var)\, f_2(d)$$

$$f_2(d) = \left(\frac{d}{d_0}\right)^{-3/m} \quad (2)$$

where m is a material parameter and $\sigma_{\lim,0}$ the mean limit strength at d_0, which is the reference diameter (here chosen as 2 mm).

To evaluate the contact area A_F in Eq. (1) Hertzian contact theory is applied. For smooth spheres the radius of the contact area is:

$$r_H = \left(\frac{3Fr'}{4E'}\right)^{1/3} \quad (3)$$

where

$$r' = \left(\frac{1}{r_1} + \frac{1}{r_2}\right)^{-1} \quad (4)$$

$$E' = \left(\frac{1-\nu_1^2}{E_1} + \frac{1-\nu_2^2}{E_2}\right)^{-1} \quad (5)$$

where r_1 and r_2 are the radius of the contacting spheres and E_1, ν_1 their elastic parameters (Young modulus and Poisson ratio, respectively).

Back substituting Eqs. (2) and (3) into Eq. (1), the limit force condition is expressed as

$$F \le \left[\sigma_{\lim,0} f_1(\mathrm{var})\left(\frac{d}{d_0}\right)^{-3/m} \pi\left(\frac{3r'}{4E'}\right)^{2/3}\right]^3 \quad (6)$$

This can be easily implemented into the PFC3D code using a FISH routine.

2.2 Particle splitting and lost mass

Once the limit condition is reached, a particle, modeled with a sphere in PFC, will split into smaller prescribed tangent spheres. It is clear that this way of modeling crushing does not conserve the mass within the numerical simulation. This is acceptable if it is assumed that the mass loss is formed by finer particles that have a small influence on the macroscopic mechanical response. Indeed, smaller particles do have a lesser role than large ones on force transmission through a granular mass (Mihn & Cheng 2013, Esnault, & Roux 2013).

With the help of auxiliary rules, the mass loss on crushing can be accounted for at the post-processing stage. For instance, the full evolution of grain size distribution (GSD) during element test can be estimated if the deleted volume is assumed to have a specific particle distribution. Here, a fractal distribution (Einav, 2007) with maximum particle size smaller than the smallest particle produced during the crushing event is assumed for that purpose.

Ciantia et al. (2015) detailed this procedure and compared the effect of an alternative splitting configurations on element test response. Authors concluded that the 14-ball crushed configuration represented in Figure 3 (47% volume of mother particle is deleted at each crushing event) was accurate enough to reproduce the macroscopic response of element tests. Since breakage only happens to a fraction of particles during test, the total volume loss for a granular ensemble is much smaller than this single-particle value (see discussion section).

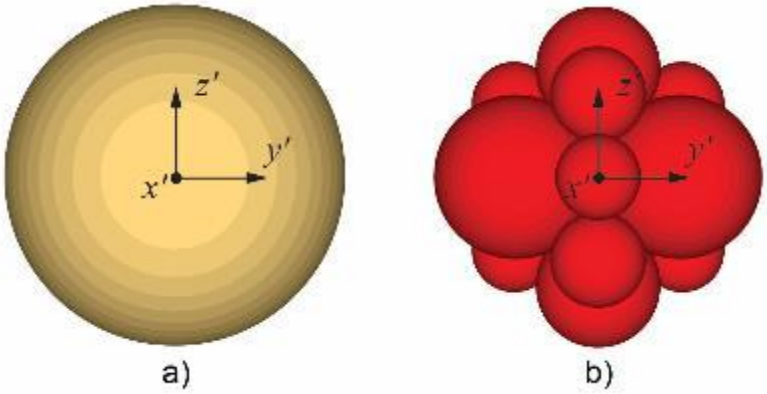

Figure 3 a) Initial particle, b) Particle splitting configuration

After breakage, the newly created particles inherit the velocity and material parameters of the mother particle except for the intrinsic strength ($\sigma_{lim,0}$) that is randomly assigned respecting normal distribution criteria. To limit the computational cost of crushing procedures in DEM it is common practice to restrict its application to particles above a certain minimum particle size, d_{limit} (Cheung et al. 2003; Marketos & Bolton, 2009; Esnault & Roux, 2013). To allow enough breakage to develop d_{limit} is always below the maximum daughter diameter of a particle with the initial median particle diameter, D_{50}.

166 **2.3 Contact model.**

167 Contacts between particles are elasto-plastic. Contact forces are limited by friction and a no-
168 tension condition

169
$$\begin{aligned} F_n &\geq 0 \\ F_t &\leq \tan\phi F_n \end{aligned} \tag{7}$$

170 where F_n and F_t are, respectively, the normal and shear contact force components, ϕ is the
171 interparticle friction angle. The simplified Hertz-Mindlin contact model is used to represent
172 non-linear contact stiffness

173
$$\begin{aligned} k_N &= \left(\frac{2\langle G \rangle \sqrt{2\frac{d_1 d_2}{d_1 + d_2}}}{3\left(1-\langle \nu \rangle\right)} \right) \sqrt{U} \\ k_S &= \left(\frac{2\left(\langle G \rangle^2 3\left(1-\langle \nu \rangle\right) \frac{d_1 d_2}{d_1 + d_2} \right)^{1/3}}{2-\langle \nu \rangle} \right) |F_n|^{1/3} \end{aligned} \tag{8}$$

174 where U is the sphere overlap, $|F_n|$ is the magnitude of the normal contact force and the $\langle\ \rangle$
175 brackets indicate the mean value of the quantity considered of the two balls in contact; G is a
176 shear modulus, ν is a Poisson ratio and d_1, d_2 are the diameters of the contacting particles.
177 Discrete element rotation was inhibited to roughly mimic the effect of the very angular shape
178 of pumice sand. This approach, which can be traced back to Ting et al. (1989), has been
179 successfully applied in previous models of angular granular materials (Arroyo et al. 2011).
180

181 **2.4 Upscaling procedure.**

182 Scaling up the particle size while maintaining constant other geometrical dimensions of the
183 problem substantially reduces the number of particles in the model (Figure 4). An upper limit
184 to particle scaling is given by the relevant dimensions of the model. A sufficiently large
185 number of particles should remain so that the granular media response is maintained in an
186 average sense.

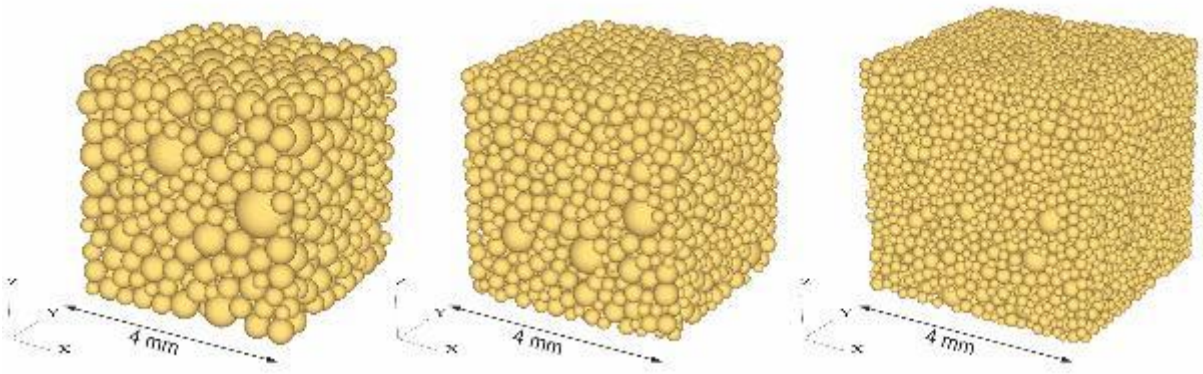

Figure 4 Scaled-up specimens for triaxial testing. (left) Scale factor = 2 corresponding to 1304 particles, (center) scale factor = 1.5 corresponding to 3084 particles, and (right) scale factor = 1 corresponding to 10397 particles.

A successful upscaling procedure should preserve the macroscopic responses of interest such as compressibility, apparent yield stress, etc. Ciantia et al. (2015) showed that this is the case for the given model if the following scaling rules are applied:

a) *Particle strength:* The scale factor N is just factored in the definition of the reference dimension d_0.

$$f_2 = \left(\frac{d}{\mathrm{N} d_0} \right)^{-3/m} \tag{9}$$

b) *Stiffness:* Gabrieli et al. (2009) reason that macroscopic stiffness is invariant on scaling if contact stiffness is proportional to particle dimensions. That is an inbuilt characteristic of the simplified Hertz-Mindlin formulation described in Eq. (8) and no modification is needed.

c) *Grain Size Distribution:* Uniform scaling of particle size shifts the GSD line towards the right proportionally to the scaling factor N. To compare GSD evolutions of the same test with different scaling factors all GSD are divided by the scale factor N (downscaling procedure).

3. Double porosity granulates

If a granular material is formed by porous grains the definition of particle mass and volume need to take that into account. An extra complication appears if the porosity of the grains varies with grain size.

3.1 Internal porosity size dependency

The reference material in this study is a Pumice sand described by Wesley (2007). Particles of this sand are almost entirely formed by quartz but, because of their internal porosity, they have an apparent specific gravity well below that of quartz (G_{s0} ~ 2.6). Moreover, the apparent specific gravity of single sized fractions is not constant. This means that intragranular or internal porosity, n_{int} is variable with particle diameter, since:

$$n_{int}(d) = 1 - \frac{G_s(d)}{G_{s0}} \tag{10}$$

Where, $G_s(d)$ is the apparent specific gravity of a particle with diameter d.

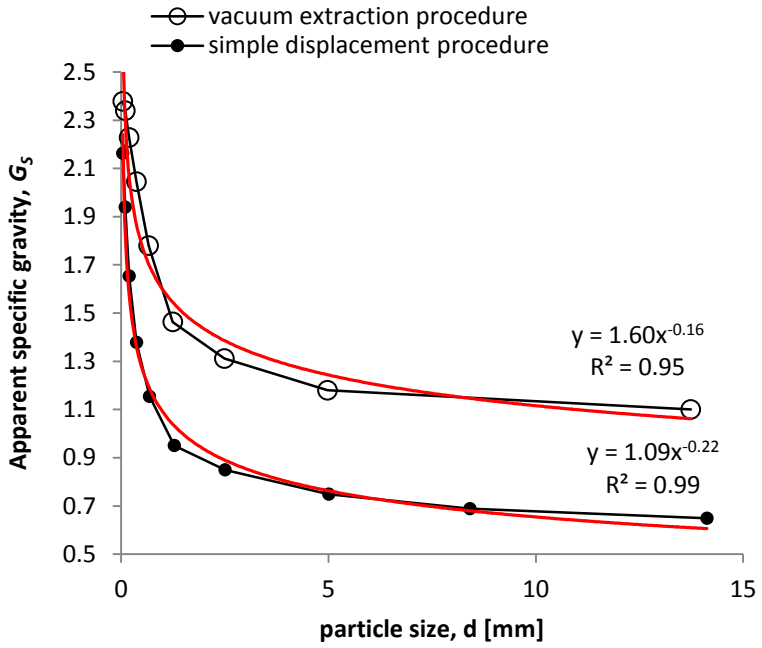

(a)

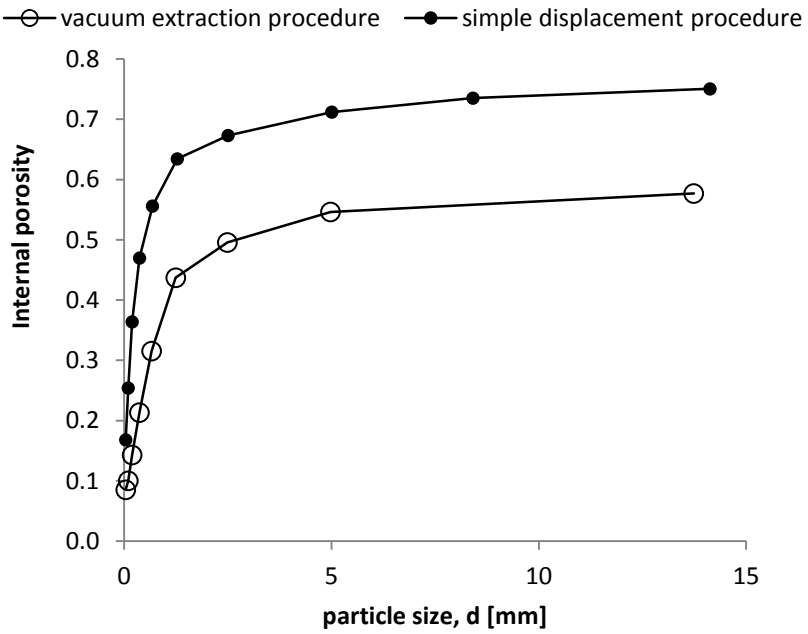

(b)

Figure 5 Crushed pumice single sized fractions a) Apparent specific gravity as a function of particle size, as reported by Wesley (2007) b) internal porosity as a function of particle diameter.

The apparent specific gravity obtained is rather sensitive to the measurement procedure (Wesley, 2001); larger values are obtained if water is forced into the surface connected porosity using vacuum than if vacuum is not applied (Figure 5a). Whatever the measurement method chosen, and similarly to other double-porosity granulates (Casini et al. 2013), the variation of specific gravity with size in this case can be well interpolated by the function:

$$G_s(d) = A\left(\frac{d}{d_{ref}}\right)^{-B} \tag{11}$$

Where d_{ref} is a reference diameter (1 mm), d is particle diameter and A, B are the curve parameters indicated in Figure 5a. Using Eq. (10) and the experimental results of Figure 5a it is possible to plot the dependency of internal porosity on particle diameter (Figure 5b).

3.2 Intergranular and intragranular porosity

To incorporate internal porosity in the DEM model, the internal porosity, n_{int} of a single particle, p, is defined as:

$$n_{\text{int}}^{p} = \frac{V_V^p}{V_T^p} \tag{12}$$

Where V_V^p is the volume of the voids within particle *p*, while V_T^p is the total volume of that particle. Therefore, the solid volume for particle *p* results:

$$V_S^p = V_T^p \left(1 - n_{\text{int}}^p\right) \tag{13}$$

And the total solid volume for a collection of *p* particles reads

$$V_S = \sum_p V_S^p = \sum_p V_S^p \left(1 - n_{\text{int}}^p\right) \tag{14}$$

When a porous granular material fills a container of total volume V_T, the intergranular porosity, n^{inter} is the total volume fraction not occupied by particles

$$n^{\text{inter}} = 1 - \frac{\sum_p V_T^p}{V_T} \tag{15}$$

And the intragranular porosity, n^{intra} is the total volume fraction occupied by internal voids

$$n^{\text{intra}} = \frac{\sum_p V_V^p}{V_T} \tag{16}$$

Total porosity is obtained as the sum of intergranular and intragranular fractions, (Casini et al. 2013; Ciantia et al. 2014b)

$$n = n^{\text{inter}} + n^{\text{intra}} \tag{17}$$

Porosity fractions are easily computed in DEM, but not so in the laboratory and some simplifications are in use. Thus, for instance, Wesley (2007) systematically assumed a constant apparent specific gravity, $\bar{G}_s$ of 1.77, or, equivalently, a constant internal porosity of

$\bar{n}_{\text{int}}$=0.32 when interpreting mechanical tests on Pumice sand. Assuming constant internal porosity introduces an approximation in the estimate of intragranular porosity. The difference between the approximate value, $\bar{n}^{intra}$, and the exact one is given by a correction term, Δn

$$\bar{n}^{\text{intra}} = n^{\text{intra}} + \Delta n \tag{18}$$

Within experimental measuring error, total porosity can be exactly deduced from dry unit weight and the material specific gravity G_{s0} as

$$n = 1 - \frac{\gamma_d}{\gamma_w G_{s0}} \tag{19}$$

By analogy, Wesley (2007) reported his tests using an apparent porosity n^*, deduced from dry unit weight, γ_d, and the assumed apparent specific gravity $\bar{G}_s$. We have then

$$n^* = 1 - \frac{\gamma_d}{\gamma_w \bar{G}_s} \tag{20}$$

It can be seen (see Appendix) that this apparent porosity value is related to the exact value of intergranular porosity by

$$n^{\text{inter}} = n^* + \frac{\Delta n}{\left(1 - \bar{n}_{\text{int}}\right)} \tag{21}$$

3.3 Internal porosity and particle generation

The same grain size distribution by weight (Figure 6a) can be obtained using very different hypothesis about internal particle porosity. However, these different hypothesis results in different particle numbers (the volumetric grain size distribution changes, Figure 6b) because initial fabric and its evolution through crushing are also dependent on particle size. The initial estimate of internal porosity variation with particle diameter has some effect in the amount of crushing induced during a test.

For all the simulations described below, DEM particles were assigned an internal porosity values deduced from simple water displacement measurements of specific gravity on crushed

single-sized fractions of pumice. These are the values reflected in the upper curve of Figure 5b. This is based on the assumption that the outside perimeter of the particle determines contact interactions. Hence surface-connected particle porosity should be included within internal element porosity. Other hypothesis may be implemented in the discrete model, if needed.

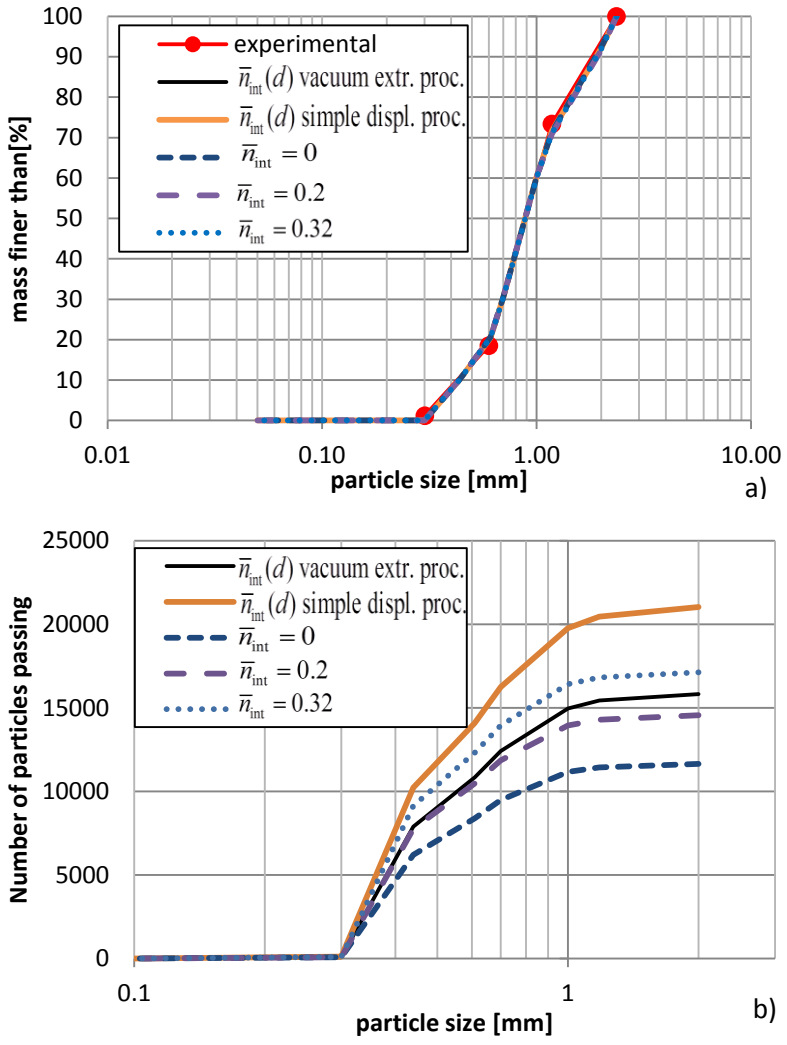

Figure 6 a) Weight cumulative grain size distribution obtained using different internal porosity hypothesis b) Corresponding particle numbers for fixed overall mass

4. Single-specimen response

4.1 Sample preparation and initial conditions

Cubical discrete specimens with 16 mm side were created using the radius expansion method (REM). Particle sizes were selected to match the weight cumulative grain size distribution taking into account the internal porosity distribution described by Eq. (11) with A = 1.09 and B = 0.22.

After REM finished, velocities were set to zero. Isotropic compression of 5 kPa was used to obtain – by trial and error, using a temporary interparticle friction reduction and disabling crushing– a closer fit to the initial intergranular porosity target, n^{inter}, of each simulation. That target intergranular porosity was obtained from Eq. (21) using the reported apparent porosity of the specimen, n^*, the $\bar{n}_{\text{int}}$=0.32 value assumed by Wesley (2007) and computing the corresponding correction term, ($\Delta n \approx$ -0.15) for the assumed internal porosity distribution.

4.2 Calibration

The parameters to calibrate are: elastic modulus, (G, ν), contact friction angle, (ϕ), mean limit strength, $\sigma_{\text{lim},0}$, strength variability for a fixed size (*var*, coefficient of variation of the limit strength) and the m modulus controlling the size effect on strength. Calibration is achieved partly by fitting the macroscopic specimen-scale response of selected laboratory tests and partly by using grain-scale information.

As detailed in Ciantia et al. (2015), grain-scale information in the form of single particle crushing tests is particularly useful to calibrate crushing variability. This seems especially pertinent in a material with size-dependent internal porosity, because it is expected that microporosity will exert a major influence in grain strength. Unfortunately, flat platen compression tests on pumice sand for different particle dimensions were not available. It was then necessary to work by analogy with other porous geomaterial: calcarenite.

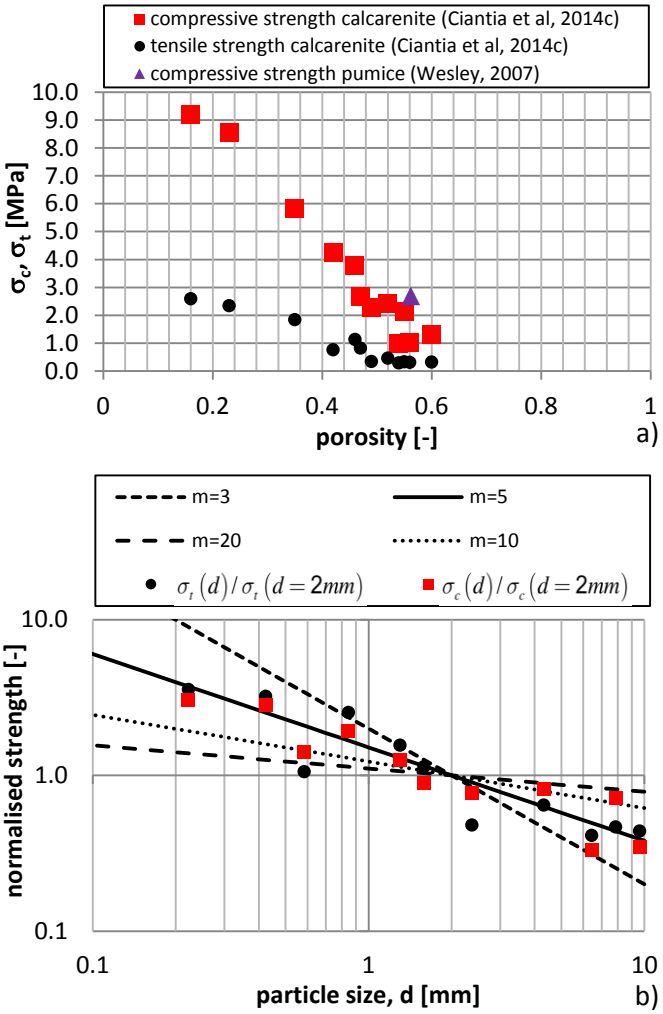

316

317

318 **Figure 7 a) Uniaxial compression and indirect tensile strength of calcarenite as a function of**
319 **porosity and b) normalized strength as a function of equivalent particle size.**

320

321 The porosity-strength relation for calcarenite rock was experimentally established
322 (Ciantia et al., 2014c) for both the unconfined compression and tensile modes of failure. Data
323 for unconfined compression on a cube of pumice rock was available in Wesley, 2007. It was
324 found that the strength of pumice sand was very close to that of calcarenite specimens with
325 similar porosity (Figure 7a). It was then accepted that the behavior of calcarenite rock
326 specimens offered a good approximation for pumice sand grains, and calcarenite results were
327 then taken as a guide to establish a particle size normalized strength dependency (Figure 7b)
328 from which a value of the *m* modulus equal to 5 was obtained for the analogue pumice sand.

329 Wesley (2007) reported results from two oedometers performed on samples with different
330 initial apparent porosity; one loose and one dense. Only the initial apparent porosity, n^*, was

reported. The total porosity and porosity fractions inferred from this value are collected in Table 1. Loose and dense DEM specimens were created to approximate the initial state of these experiments. Their initial conditions are also reported in Table 1.

Several parameters of the contact model were adjusted by fitting model response to the observed response of the loose specimen. Contact friction and elastic properties of the discrete particles (G and ν) were selected using the pre-yield section of the oedometric curve. The mean limit strength and within-size strength-variation (parameter *var*) were selected to fit the macroscopic oedometric yield stress and post-yield slope. The best fit parameters are listed in Table 2. Figure 8 show the comparison of the macroscopic response observed in the experiments and numerical simulations.

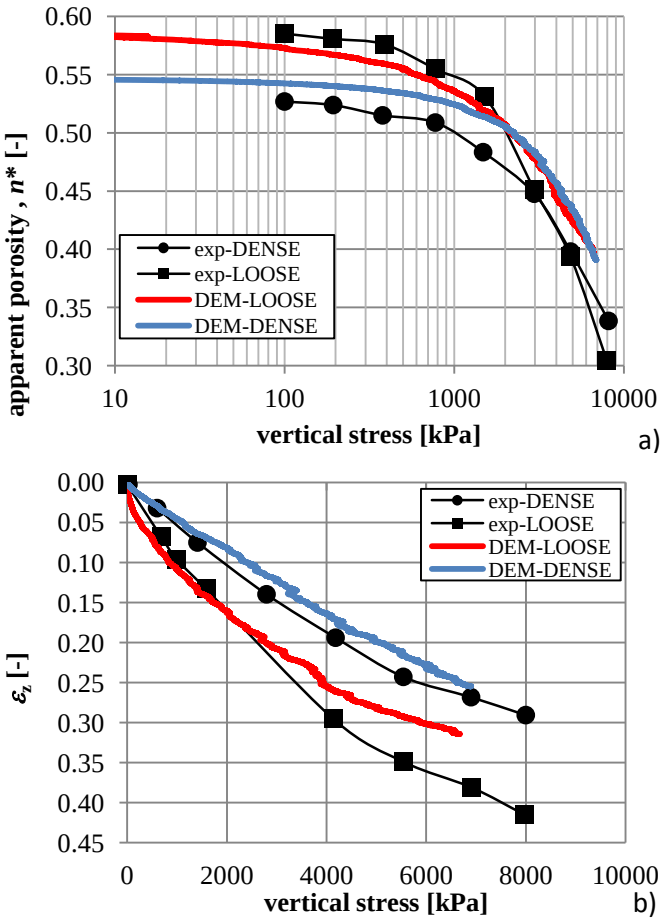

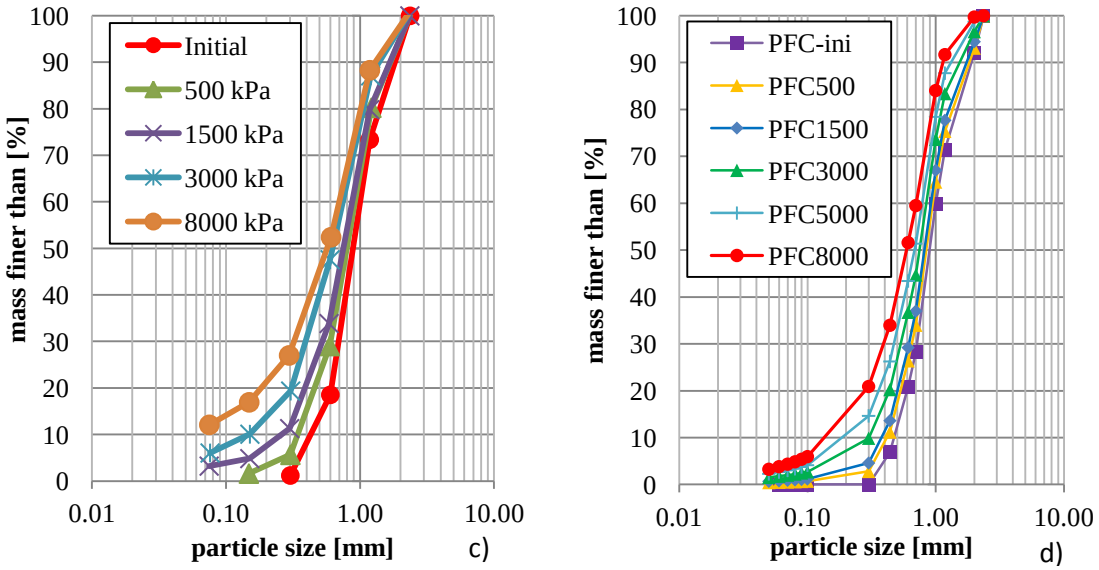

Figure 8 One dimensional compression of pumice sand: evolution of a) apparent porosity *n, b) volumetric deformation and c) experimental and d) numerical GSD of the loose sample with vertical stress.**

4.3 Validation

For validation, the oedometric response of the dense specimen was simulated. The results showed a reasonable agreement with the experimental response (Figure 8). To obtain further validation alongside a different stress path, a series of triaxial compression tests reported by Wesley (2007) at two confining pressures (50 and 300 kPa) on "loose" and "dense" specimens were also simulated. The initial porosity of "loose" and "dense" triaxial specimens was not reported, and it was therefore assumed equal to that of the corresponding oedometric tests. The numerical simulation results are reported alongside the experimental data in Figure 9. Despite some differences, the main traits of the experimental response appear to be well captured by the simulations.

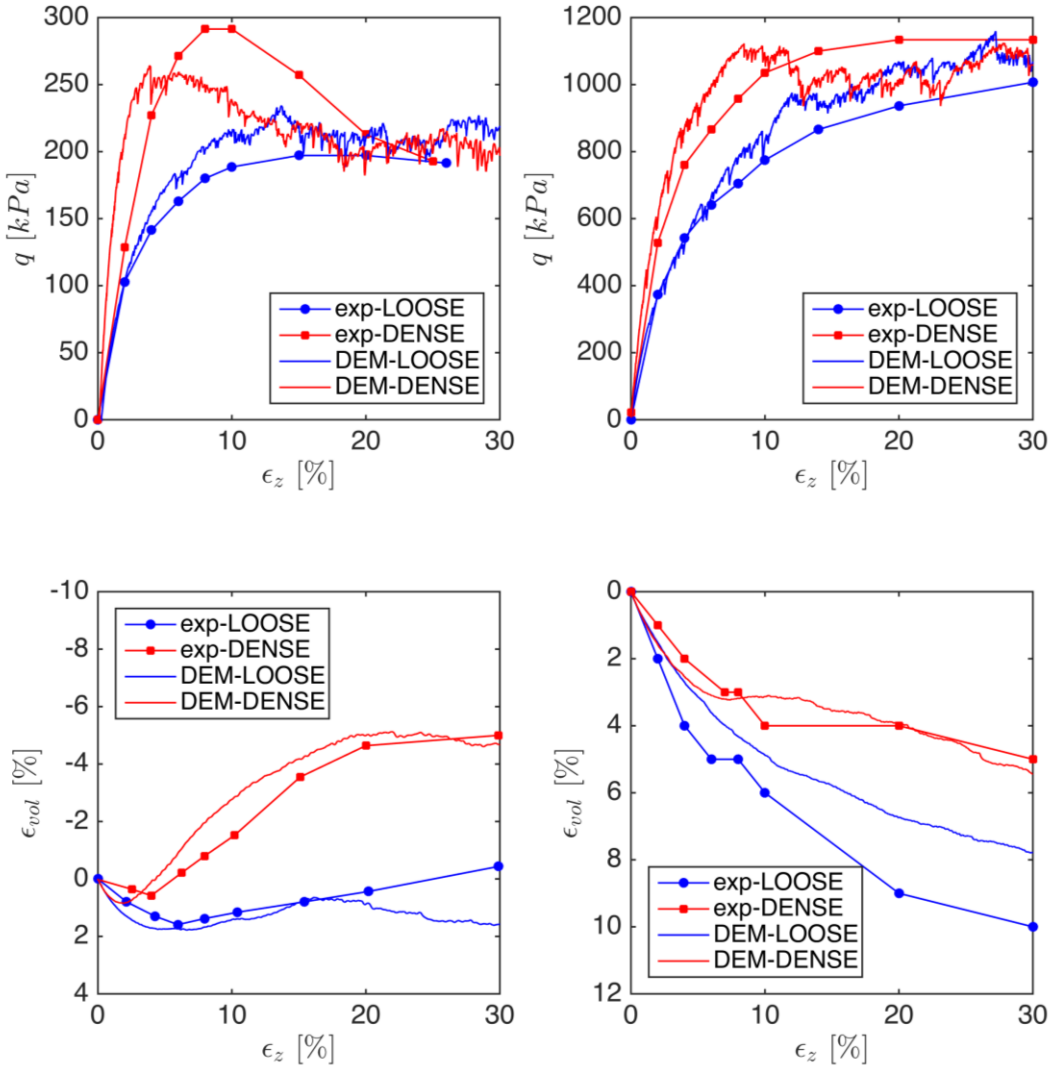

a) 50 kPa b) 300 kPa

Figure 9 Comparison of experimental and numerical triaxial results of loose and dense pumice sand prepared at confining stress of a) 50 kPa and b) 300 kPa (ε_z, ε_{vol} are the axial and volumetric strains respectively and q is a deviatoric stress)

5. Cone penetration test in pumice sand

5.1 Model construction

The calibration chamber (CC) models for CPT were built adapting the procedure described by Arroyo et al. (2011) and Butlanska et al. (2013) to represent, as closely as possible, the conditions used by Wesley (2007) in his physical experiments. A balance between realistic representation and computational affordability is necessary in this type of simulations, because computing time can increase very fast with particle numbers (e.g. McDowell et al. 2012).

In the experiments (Wesley, 2007) pumice sand was placed at the desired density by dry pluviation (loose specimens) or by layered dynamic compaction (dense specimens). Mimicking these procedures in DEM is unpractical; instead the cylindrical chamber was filled with the scaled-up material using the radius expansion method (Itasca, 2010).

To further reduce computational cost one possible approach is to take profit of the cylindrical symmetry of cone and chamber. Frictionless radial walls preventing circumferential motion of particles can be used to enforce this symmetry (McDowell et al., 2012; Lin & Wu, 2012). Arroyo et al. (2013) showed that rigid radial walls to limit model extent produce some bias towards higher cone resistances. It was thus deemed preferable to optimize model cost only by scaling up some basic problem dimensions. The main dimensions of the experimental and virtual calibration chambers are compared in Table 3. The largest difference between experiment and simulation is the scaled particle size distribution. A factor of 25 is applied to increase particle size in the CPT simulations. The cone size was also scaled-up, by a factor of 2, to obtain a cone/mean particle ratio, n_p close to 3, similar to the one employed by Arroyo et al. (2011). As shown there, and discussed in more detail elsewhere (Butlanska et al. 2013; Butlanska, 2014b) the main effect of a low n_p ratio on the simulation is to increase the noise of the raw penetrograms, which become very jagged. The noise can be filtered out by fitting an appropriate penetration trend line. The following exponential trend has been successfully applied before for that purpose (Arroyo et al. 2011):

$$q_c(h_p) = a[1-\exp(-b\,h_p)] \tag{22}$$

where q_c [MPa] is a cone resistance, h_p is a penetration depth and a & b are fitting parameters. Parameter a [MPa] gives the asymptotic or steady state value of cone resistance.

The scaled up cone-size resulted in a chamber/cone ratio, R_d, which was half of that applied in the experiments. The implications of this difference are discussed later.

The scaled discrete material filled the chamber with approximately 5.5×10^4 particles. A dimensional analysis of this case similar to that presented in Butlanska et al. (2010b) indicates that, if particle size was not scaled, the number of initial particles filling the chamber would increase by four orders of magnitude. The chamber and cone employed in the simulations are illustrated in Figure 10

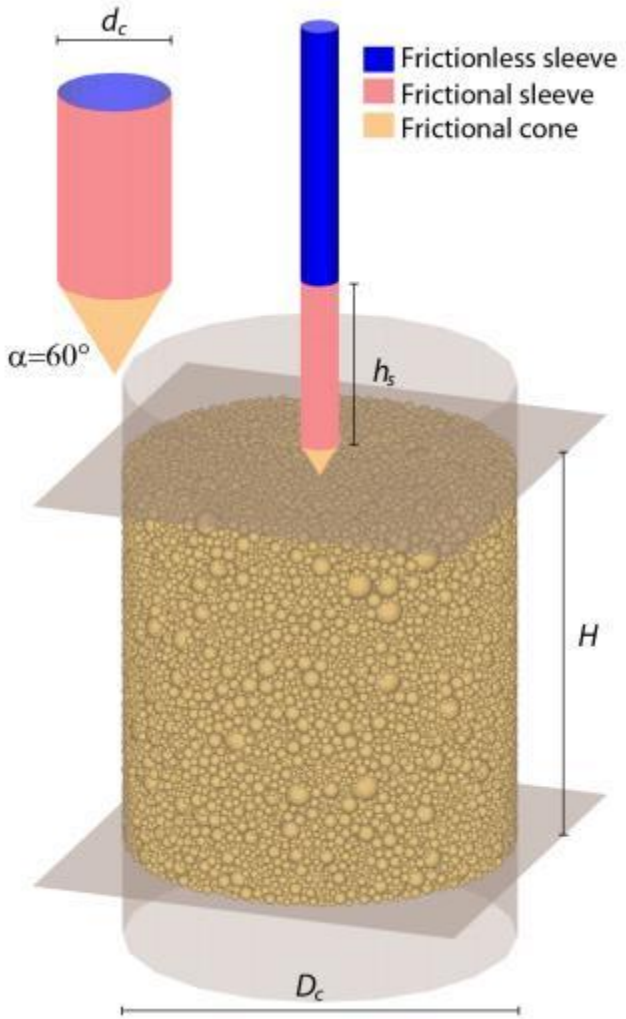

Figure 10 Example geometry before CPT

5.2 CPT simulations

The calibration chamber CPT described by Wesley (2007) were performed under a no-strain radial lateral condition (BC3: σv=constant, εr=0), with vertical stress constant at the base and a rigid wall on top through which the cone passes. These conditions were replicated in the model, although rigid frictionless walls were used instead of membranes. The bottom horizontal wall is servo controlled to apply the desired vertical stress level.

The cone shaft was modelled using rigid cylindrical walls which, as illustrated in Figure 10, were frictional close to the tip and frictionless far from it. The tip had an angle of 60 degrees and was also frictional with a tip-particle friction coefficient set equal to the interparticle friction. Cone penetration was simulated at a rate of 10 cm/s. Butlanska et al. (2010a) showed that rates between 2 and 50 cm/s do not change the simulation result. The chosen penetration rate is also below the 1 m/s limit where dynamical effects are apparent (Quezada et al., 2014; Tran et al., 2014). All the simulations employed a local non-viscous damping coefficient of 0.05.

Table 4 collects the conditions reported by Wesley (2007) for six CPT tests on pumice sand, alongside those prevailing in the simulations. The test conditions combine two density levels, namely *loose* and *dense* and three vertical stress levels. In the experiments both *loose* and *dense* conditions varied significantly and were looser than the equivalent conditions for the specimen tests (Table 1). For simplicity, the CC DEM specimens were all formed at two initial densities (at 5 kPa) used for the element tests. After equilibration stage, one-dimensional compression was performed until the target value of vertical stress was attained. The horizontal stress was finally adjusted using a radial wall servo-control until the system was again in equilibrium. A parallel series of 6 CPT DEM tests were performed in specimens formed at the same initial density and taken to the same stress level, but in which particle crushing was not allowed.

5.3 Macroscale results

The main result of interest here are the values of cone tip resistance. Figure 11 collects the penetrograms from all the simulations as well as the adjusted penetration curves. Table 5 summarizes the parameters of each adjusted penetration curve. The steady state values of

cone resistance (given by the *a* parameter of the adjusted penetration curve) are plotted against applied vertical stress in Figure 12.

As expected, the small cone diameter-to-mean particle ratio, n_p, results in noisy penetrograms with very strong oscillations (Figure 11). The penetration curves, however, reveal some clear trends. In the crushable material initial density has no discernible effect on cone resistance; when crushing is disabled cone resistance in the denser material roughly doubles that of the looser one. Increasing the boundary vertical stress does increase cone resistance for both the crushable and uncrushable materials, but it does so at a much faster rate in the non-crushable material, particularly if the initial state is dense (Figure 12).

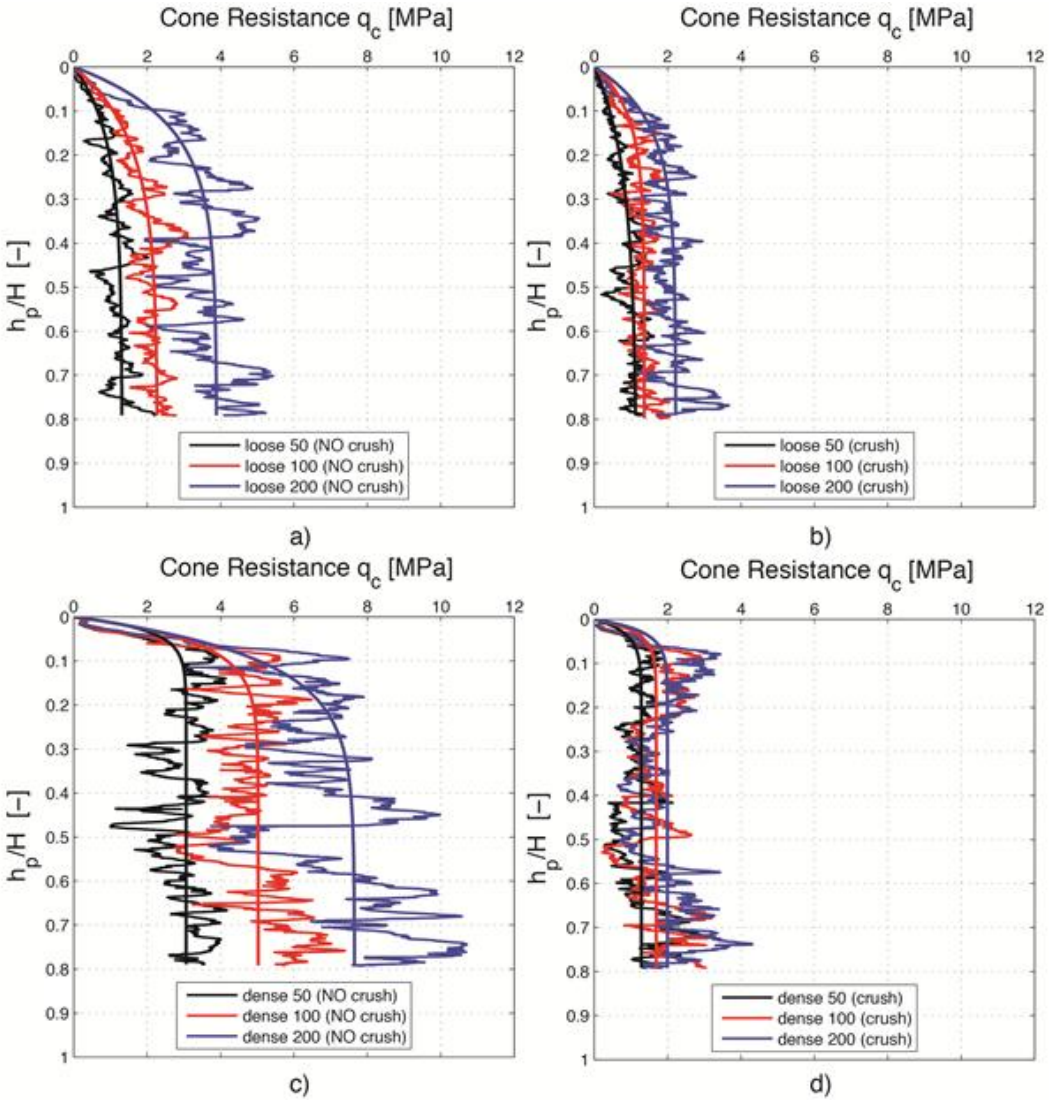

Figure 11 Raw penetrograms and adjusted penetration curves (a) loose uncrushable material (b) loose crushable material (c) dense uncrushable material (d) dense crushable material

448

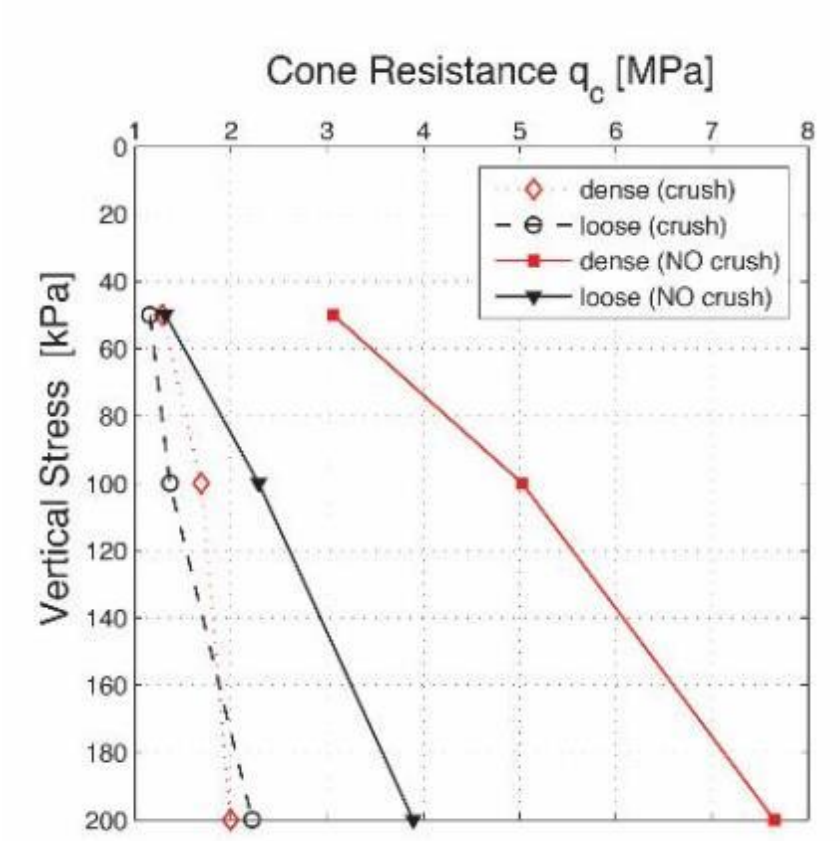

449

450 **Figure 12 Steady state values of cone resistance vs vertical stress at the base**

451 **5.4 Microscale observations**

452

453 As explained by Butlanska et al. (2013) the results of DEM CPT simulations can be
454 examined at several scales. Macroscale results are whole-system responses of direct
455 engineering interest, like the cone tip resistances examined in the previous section. The
456 micro-scale level of resolution describes variables at the highest possible resolution, that is, at
457 the particle or contact level. The variables described at this level are usually discrete, but they
458 might be also continuum inspired, like particle stress. Particle stress is a representative or
459 notional average grain stresses, computed from contact forces (O'Sullivan, 2011).

460 Figure 13 represents, for a vertical slice of the CC, the vertical particle stress component
461 side by side with the network of contact forces (CF) at the same stage. Forces exceeding the
462 whole ensemble average (μ) are plotted in dark grey if CF< μ +5σ while they are in black

463 if CF> μ +5σ where σ is the standard deviation. The forces smaller than the average force
464 are plotted in light gray. The lines join the centroids of contacting spheres and their thickness
465 is proportional to the magnitude of the normal force.

466 When the CPT is performed in a loose material under 100 kPa, many free spaces are
467 visible within the granular mass. Particles are less constrained when pushed by the cone and
468 zones of highly stressed particles are then relatively small. Differences between the crushable
469 and non-crushable case, almost negligible at the macroscale, (Figure 12), are also small at the
470 microscale. The contact force networks of the uncrushable and crushable material appear very
471 similar also in correspondence of horizontal sections above (section A-A*) and below (section
472 B-B*) of the cone tip (Figure 14).

473 The situation is different for the CPT on the denser specimens (Figure 15). A cluster of
474 highly stressed particles appears below the cone tip in this dense case. The size of this cluster
475 is far larger in the non-crushable material than in the crushable one. The strong contact force
476 network appears rarefied in the crushable material just in the area below the tip where the
477 highest particle stresses appear in the uncrushable material (section B-B*, Figure 16). This
478 suggest that it is in that particular zone crushing takes place (CPT induced). In the non-
479 crushable material strong force chains that emanate from the cone tip are able to reach further
480 into the chamber. When crushing is enabled the vertical pattern of strong force chains
481 associated with the chamber principal stress axis appears less disrupted by cone intrusion.
482 Behind the cone tip (section A-A*, Figure 16) the rarefication of strong force chains in the
483 crushable case is also clear. The implications of this for side friction are outside the scope of
484 this paper.

485 Crushing takes place both before CPT (during initial chamber stress set-up) and during
486 cone penetration. It is interesting to compare the spatial localization of the crushing events
487 that take place during these two separate simulation phases. In Figure 17 the location of
488 crushed particles in two orthogonal chamber slices is represented for the compression phase,
489 previous to CPT, in the dense specimen under 200 kPa. It is apparent that crushing events are
490 evenly distributed within the chamber. Representing now only the particles crushed during the
491 CPT phase for the same test a very different pattern appears (Figure 18). Most crushing events

have taken place within 2-3 radius from the cone. This is in agreement with the pattern suggested by the force network and particle stress in Figure 15.

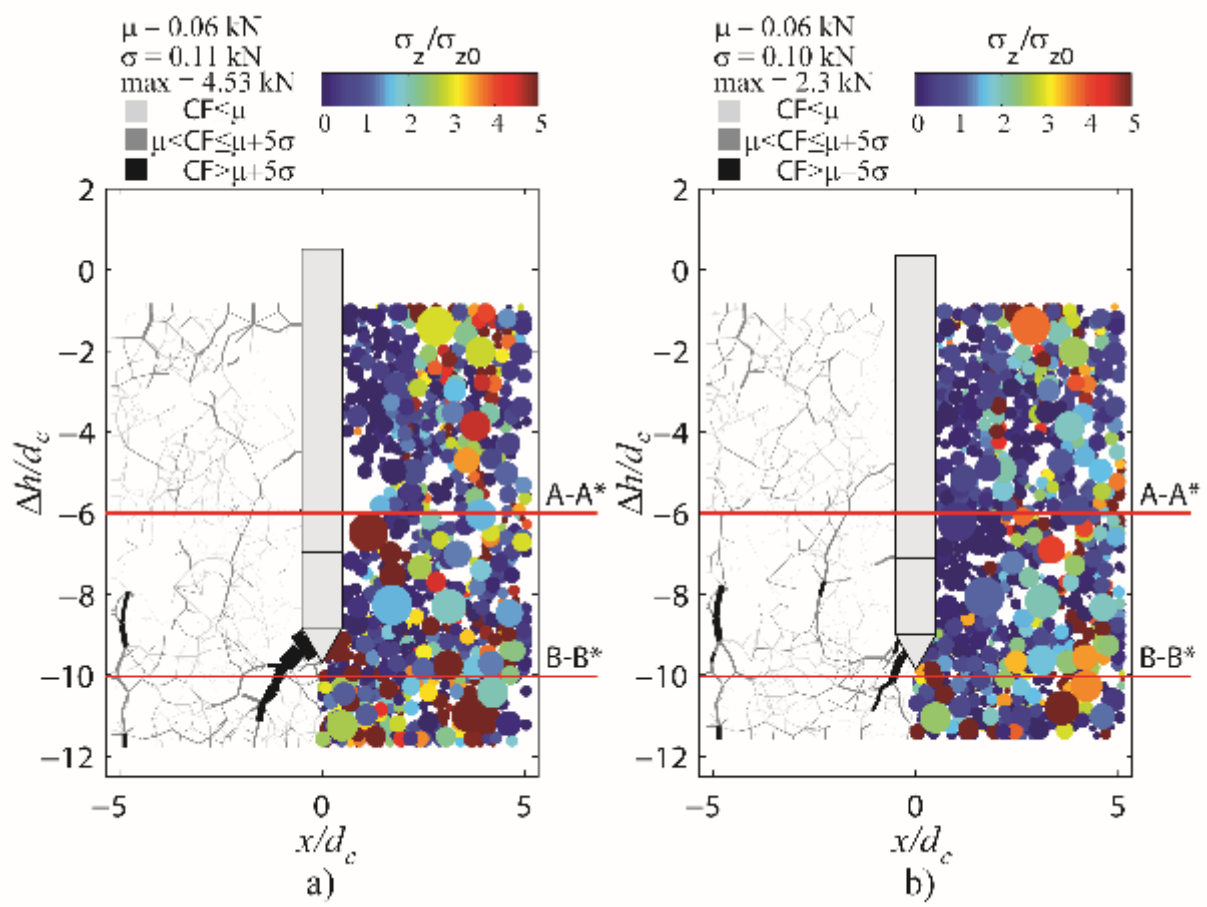

Figure 13 CPT on a) uncrushable and b) crushable loose specimens at σ_{z0} = 100 kPa applied vertical stress. Left half: contact forces. Right half: particle vertical stress normalised by applied vertical stress σ_{z0}.

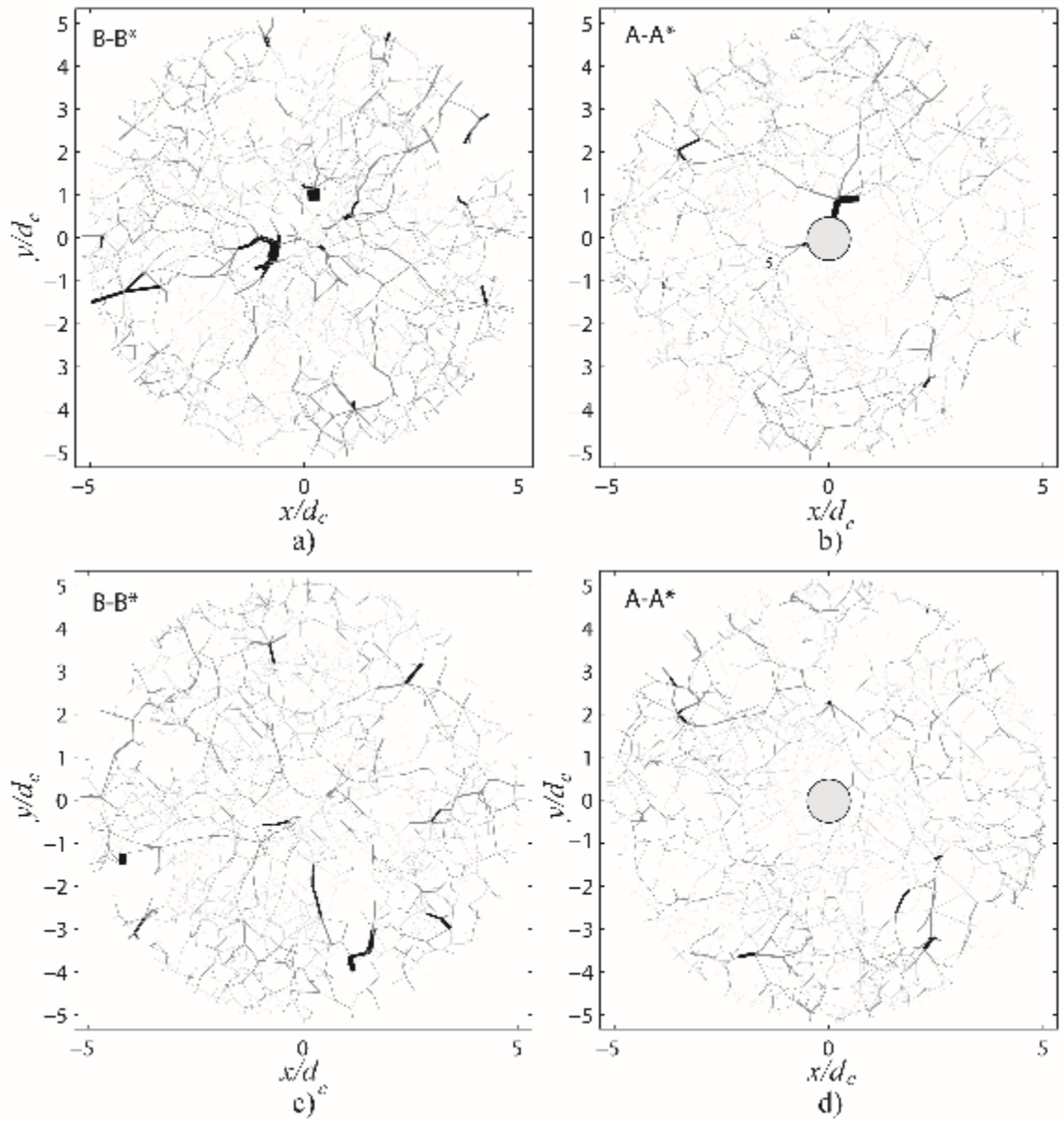

Figure 14 Particle contact forces for loose uncrushable (a,b) and loose crushable (c,d) in sections A-A* and B-B* shown in Figure 13.

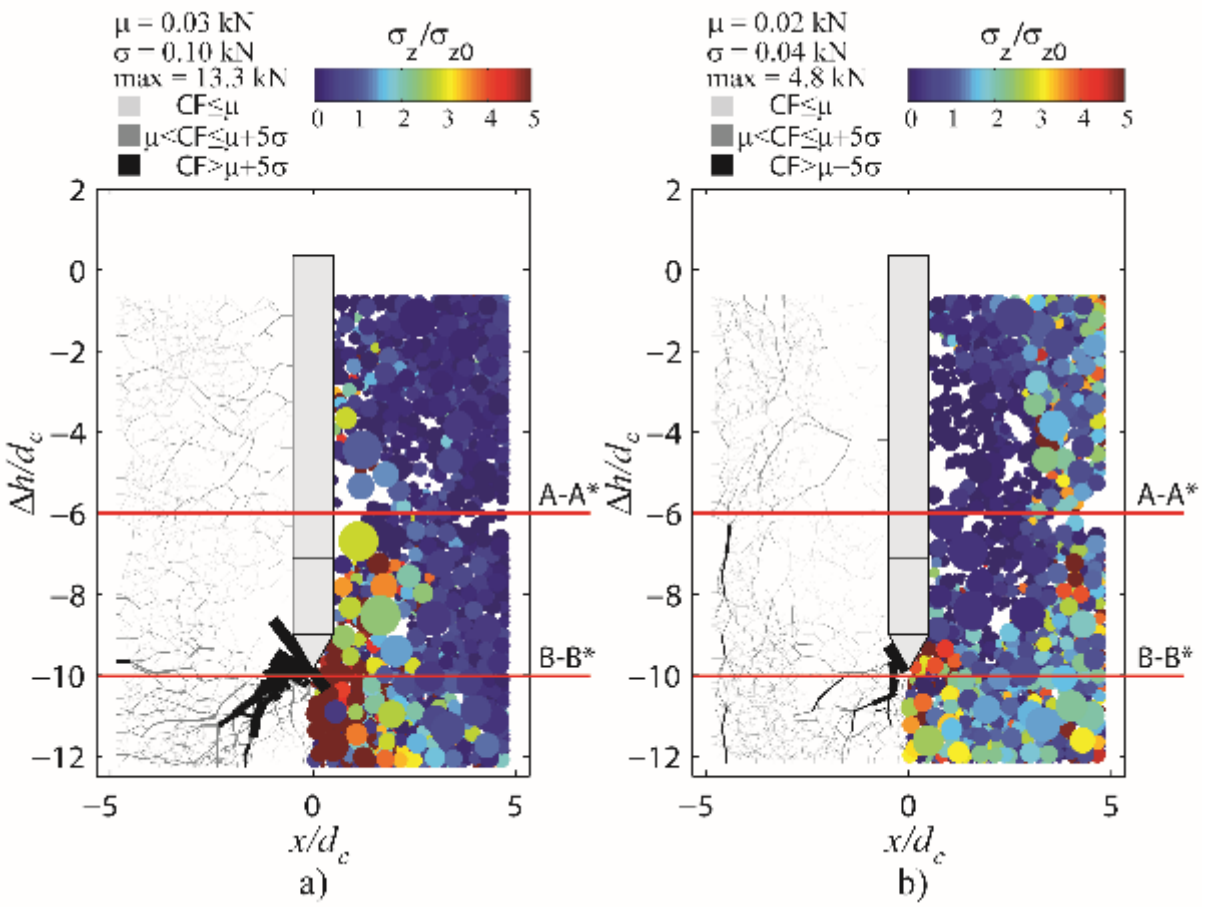

Figure 15 CPT on a) uncrushable and b) crushable dense specimens at σ_{z0}= 100 kPa applied vertical stress. Left half: contact forces. Right half: particle vertical stress normalised by applied vertical stress σ_{z0}.

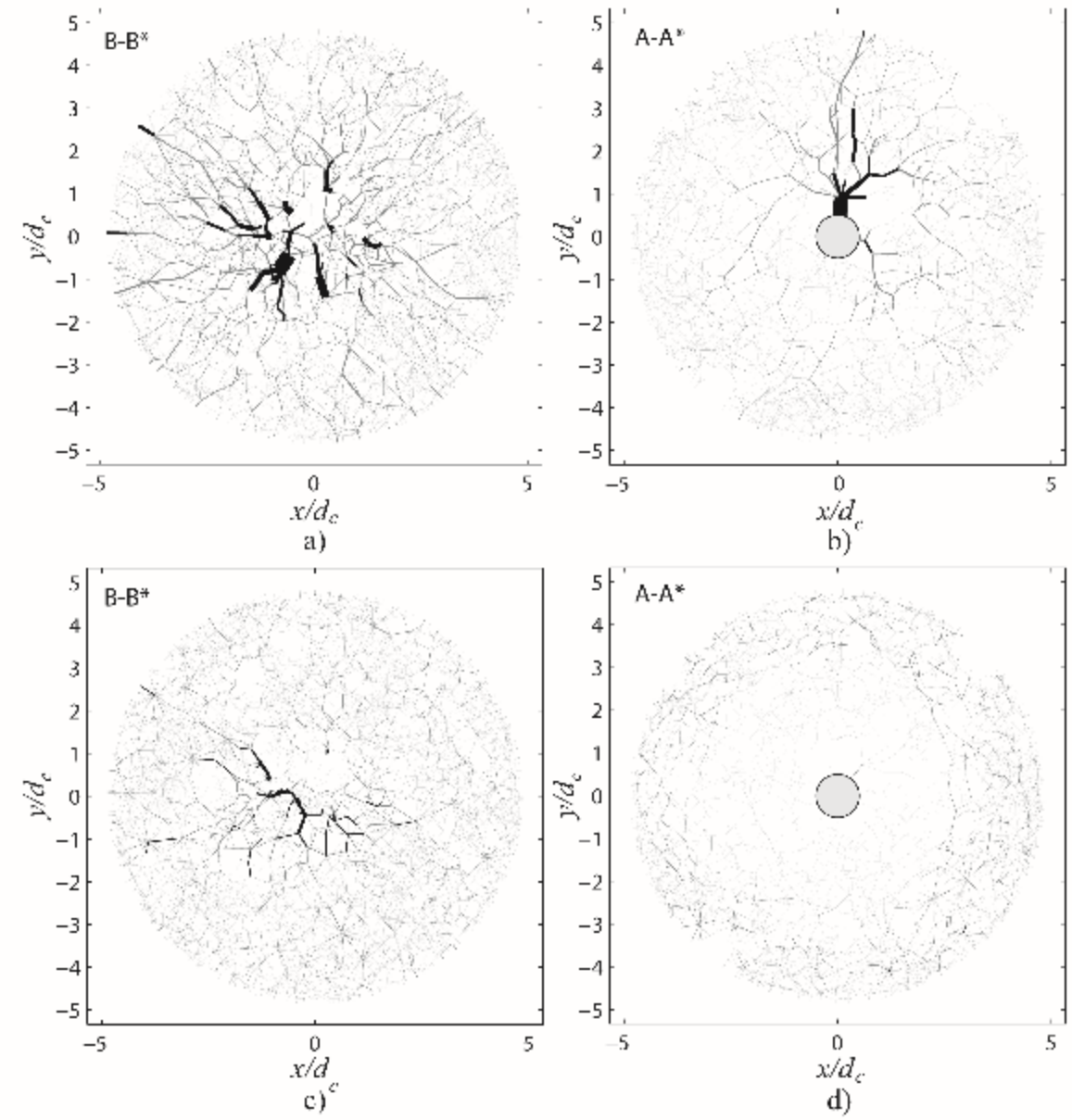

Figure 16 Particle contact forces for dense uncrushable (a,b) and dense crushable (c,d) in sections A-A* and B-B* shown in Figure 15

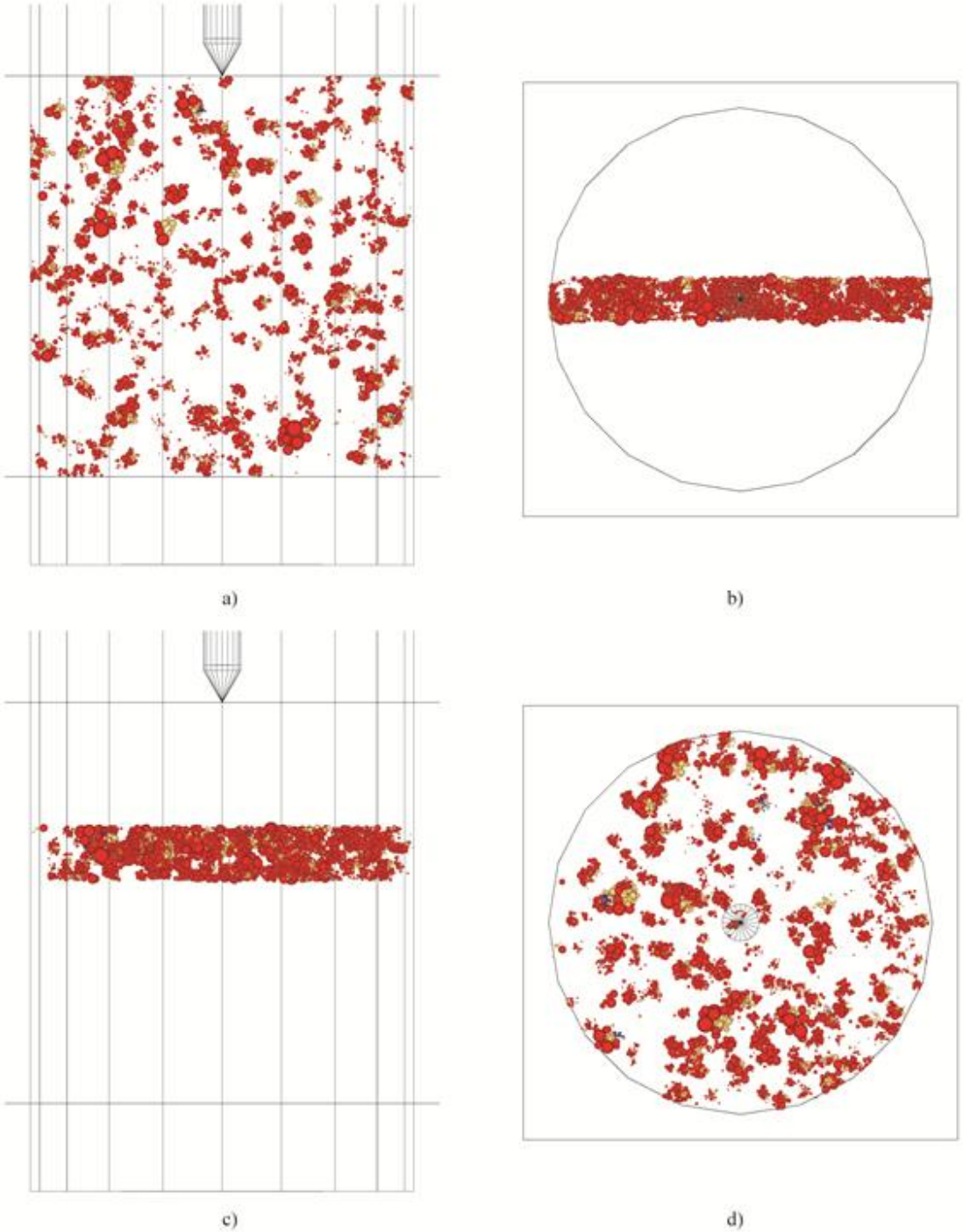

Figure 17 Crushed particles during stress initialization (before CPT) for the dense specimen at vertical stress 200 kPa (a) horizontal projection of particles crushed within a vertical slice (b) vertical projection of particles crushed within a vertical slice (c) horizontal projection of particles crushed within a horizontal slice (d) vertical projection of particles crushed within a horizontal slice.

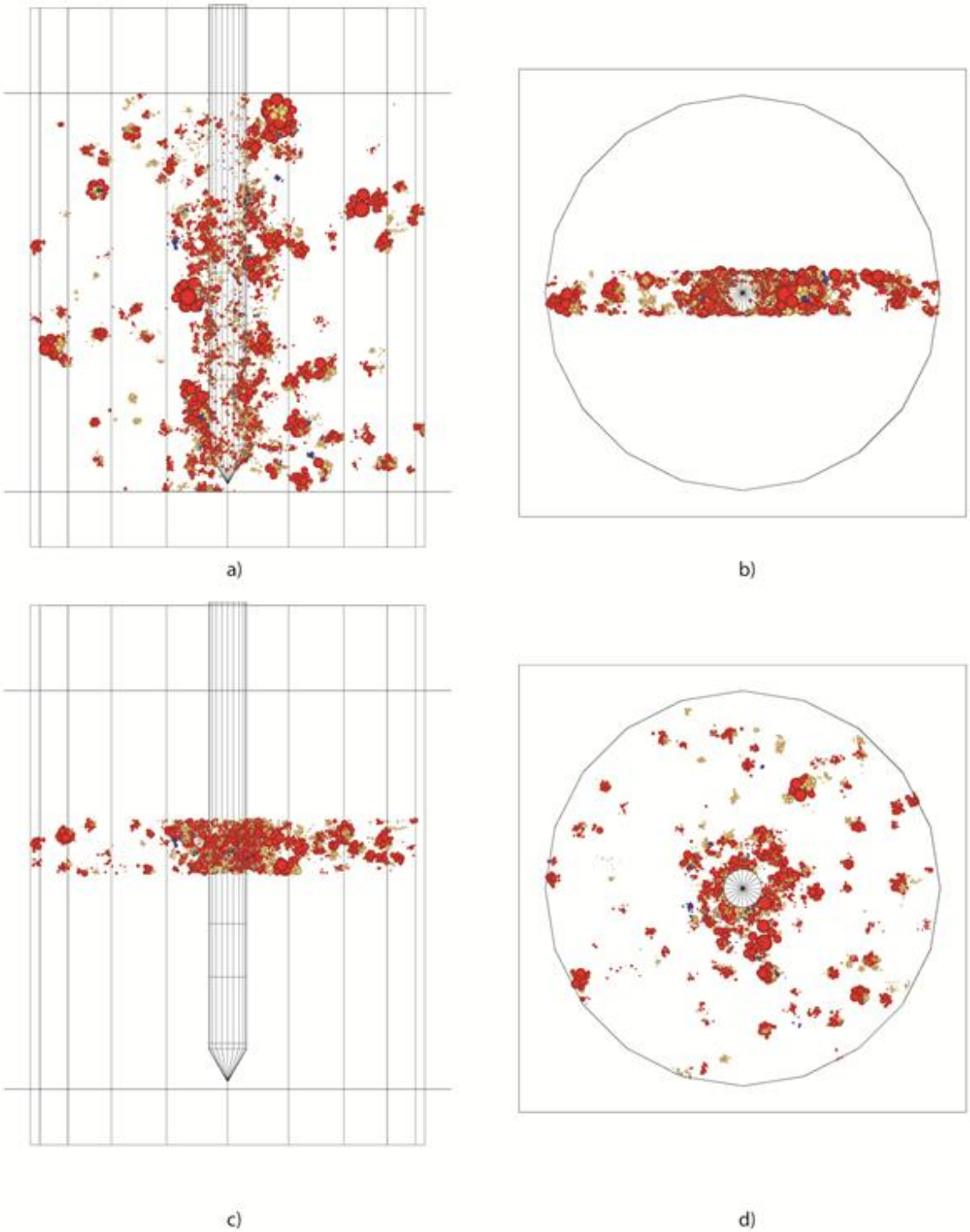

Figure 18 Crushed particles during CPT for the dense specimen at vertical stress 200 kPa (a) horizontal projection of particles crushed within a vertical slice (b) vertical projection of particles crushed within a vertical slice (c) horizontal projection of particles crushed within a horizontal slice (d) vertical projection of particles crushed within a horizontal slice.

6. Discussion

The simulations resulted in values of cone tip resistance that, as observed by Wesley (2007), were practically insensitive to initial density. When crushing is disabled in the numerical simulations cone tip resistance is multiplied by a factor ranging between 1 and 4, a factor that increases with density and vertical confinement stress. Both Almeida et al. (1991) and Wesley (2007) reported comparisons of CPT in crushable sand with parallel tests in less crushable materials. Of course, in their experiments two different sands were compared (Ticino and Quiou for Almeida et al.; Silica and Pumice for Wesley (2007)), and other factors might have changed, whereas in the simulations here the only change was that of crushability. When plotted against initial relative density, the ratios obtained in the simulation compare well with those observed in the experiments (Figure 19). Note that relative density for the Wesley (2007) CC data is obtained as average of that reported for same stress silica and pumice tests. Relative density values for the DEM simulations are assigned assuming valid the extreme γ_d values for pumice (620 and 730 kg/m^3) reported in Wesley (2007). The different specimen formation procedures followed in the laboratory and in the simulation explain DEM values are above 100%

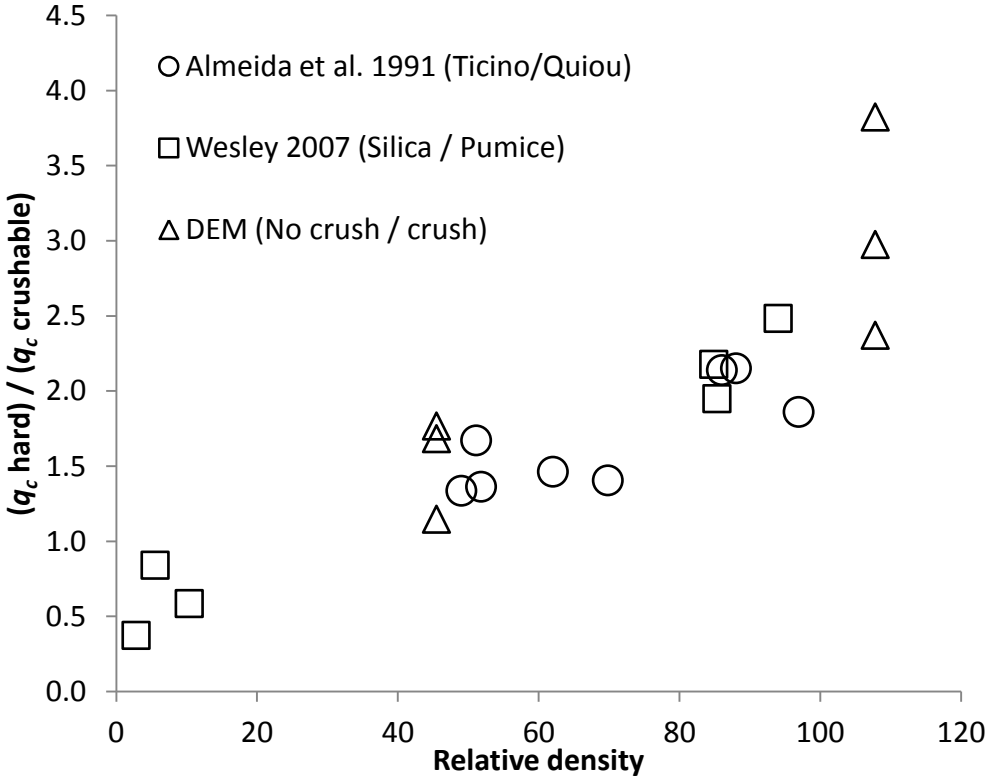

Figure 19 Effect of crushability on cone tip resistance.

Despite these remarkable coincidences, the magnitude of cone tip resistance for the crushable material in the simulations is smaller, approximately by a factor of 3, than that observed by Wesley (2007) in his experiments (compare, for instance, the result in Figure 1 to the similar test in Figure 11). There are several possible causes that explain that discrepancy. Three that seem important are (a) parameter calibration (b) mass loss (c) scaling.

The calibration process described was only approximate, lacking for instance particle-scale crushing information for pumice sand. The performance on the model in the element tests was acceptable, but, for instance the peak strength of the dense triaxial specimen was somewhat underestimated, by some 10% (Figure 9). This may have impacted on the CPT results but it is unlikely to explain most of the observed difference.

In the experiments there was no mass loss on crushing. To check the effect of lost volume in the CPT simulations, some replica tests were run. In the replica tests a particle that reached the crushing condition was simply deleted from the simulation instead of partly replaced with 14 smaller particles. This more than doubled the percentage of particle volume lost at each crushing event. The effect of that modification on the penetration curves was small (Figure 20).

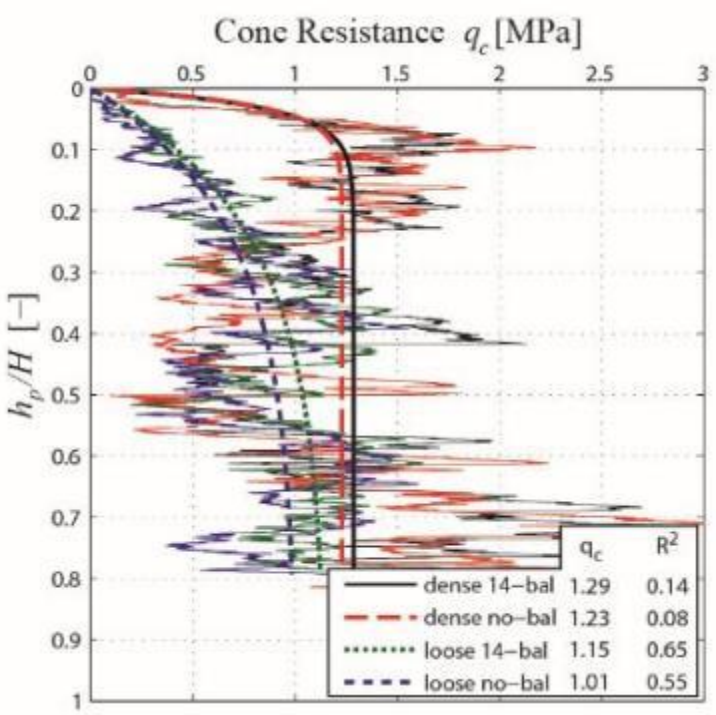

Figure 20 Effect of the mass loss upon breakage on the penetration curves for the cases when vertical stress is 200 kPa.

In fact, the mass loss during the simulations is also relatively small. Table 6 compiles the percentage of crushing events during the simulations. The number of initial particles that is crushed during the simulations remains always below 3.5% of the initial number. The percentages of crushing events during the CPT phase do not seem very sensible to initial density or boundary stress. Crushing of the original particles is larger during the initial stress installation phase, than during the penetration phase. The amount of loss mass during the simulations is consequently small, always below 5% in total and below 2% during the actual penetration test.

With respect to scaling there are two different aspects to consider. Scaling of particle size is unlikely to have much effect per se: Arroyo et al. (2011) obtained closer agreement with experimental results using a larger scaling factor (50). On the other hand, at least a sizeable part of this discrepancy can be attributed to the different chamber to cone diameter ratio, (R_d, see Table 3).

It is well known that the R_d ratio has a major effect on the penetration value in a way that depends on the specimen density and boundary conditions applied in the chamber (Butlanska

et al. 2010b). Several corrections have been proposed in the literature to account for R_d effect (Mayne & Kulhawy, 1991; Jamiolkowski et al. 2003). Most results referred to stress-controlled conditions, but Parkin and Lunne, (1982) while testing dense silica sand under no lateral strain conditions, indicated a factor of 2 in cone resistance as R_d doubled from 25 to 50. Here the experimental R_d also doubles that of the numerical model; it is then possible that chamber/cone size effect would explain most of the observed difference between experiments and simulations.

To further explore this hypothesis a numerical experiment was devised. A new virtual chamber (Table 3, column "DEM Large") was built using a non-scaled cone to obtain the same R_d = 21 that was prevailing in the experiments. A smaller cone required a smaller particle scaling factor, to keep cone/particle ratio large enough. This resulted in a computationally costly model (more than 2×10^5 first generation particles).

This larger model was run at high density under vertical confinement of 50 and 200 kPa, with and without crushing. Aligned with previous results, the reduction on q_c induced by crushing in this large chamber case is given approximately by a factor of 2 (Figure 21a,b). For the 200 kPa case, the full experimental curve was available. A very good match with the corresponding numerical simulation is observed. Chamber/cone relative size has a dominant role (Figure 21c,d) explaining the differences noted before between the absolute values of tip resistance in the experiment and in the main simulation series.

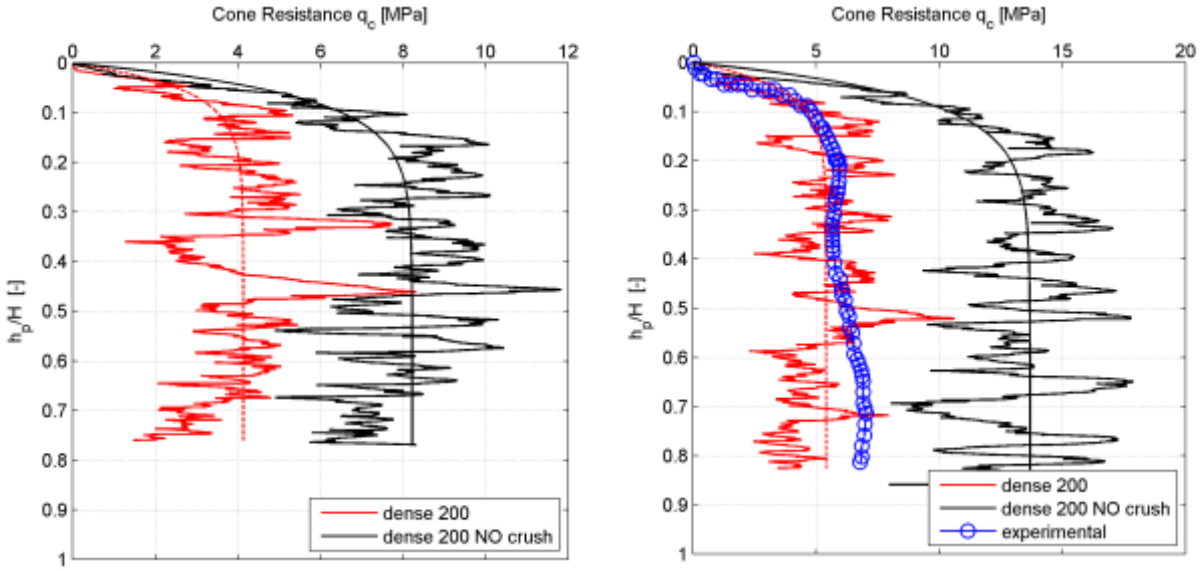

(a) σ_{z0}=50kPa

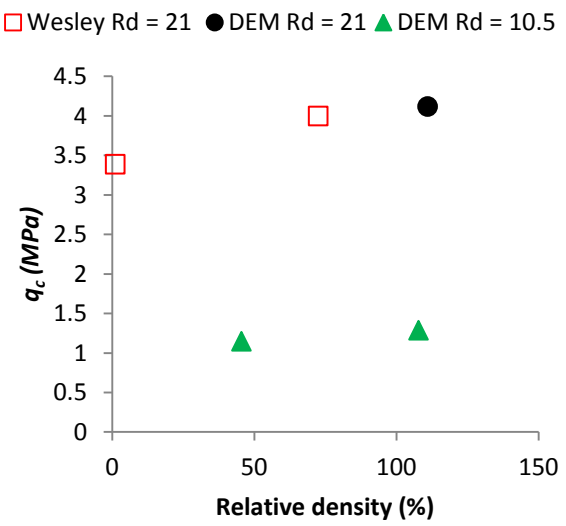

(b) σ_{z0}=200kPa

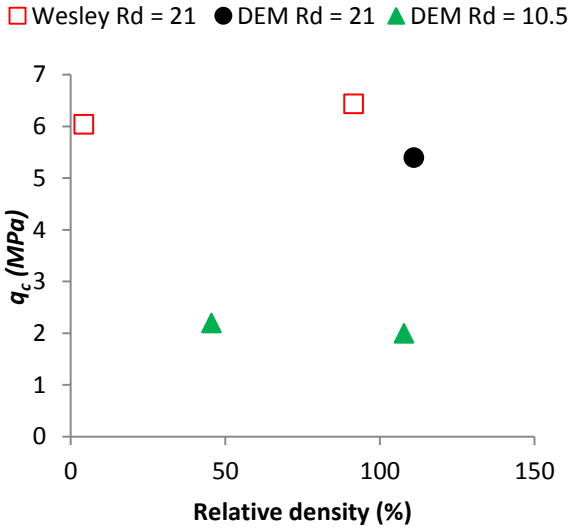

(c) σ_{z0}=50kPa

(d) σ_{z0}=200kPa

Figure 21 Chamber/cone size effect: (a)-(b) Raw and adjusted penetration curves for CPT performed in crushable and uncrushable material under two different confining stress, σ_{z0}=50kPa and 200kPa, respectively; (c)-(d) adjusted cone tip resistance values for the tests shown above.

7. Conclusions

It has been shown how analogue discrete models of crushable soils can be built using enhanced DEM models. Soils may crush even without having porous grains, but soils that have porous grains are generally more crushable. Incorporating internal grain porosity requires a proper definition of porosity fractions and some attention to the fact that internal porosity may be grain-size dependent. It is perhaps more difficult to exactly measure such dependency in experiments than to incorporate it into a discrete model.

Extrapolation of single-specimen behavior to calibration chamber behavior requires scaling to limit computational costs. Scaling makes the comparison with experimental CC tests difficult, because some important geometric ratios of the problem are changed. Numerical chamber filling procedures are unlike experimental ones and may produce different fabrics and result in somewhat inhomogeneous specimens. Despite all these severe procedural limitations, it appears that the effect of crushability on cone tip resistance that is predicted by the simulations here presented is remarkably similar to what has been observed on previous experimental work. Thus the DEM analysis results in cone tip resistances that are practically insensitive to initial density. Also, the computed ratio between cone tip resistance of non-crushable and crushable pumice sand is quite similar to reported experimental values over a range of relative densities. Quantitative agreement was also obtained with Wesley's experimental tip resistance results running models with a non-scaled cone.

Macroscopic agreement with experimental observations offers credence to microscopic observations that are simply extracted from discrete models but which have difficult direct experimental verification. A limited amount of microscale exploration of the simulations has been presented here. It suggests that most particle crushing during cone penetration occurs at some distance below the cone tip. It does also indicate that crushing reduced the length of the strong force chains radiating from the cone tip into the chamber. Crushing also disrupts the strong force network behind the cone tip, close to the shaft, where newly created particles accumulate. The microscopic results suggest that in crushable soils the cone feels mostly the material that its own insertion has created. The effect on simulated cone shaft resistance of crushing is currently under investigation.

Finally, it is noted that, although not directly addressed here, similar observations on the effect of crushability on driven pile tip resistance have been reported (e.g. Kuwajima et al. 2009). It is then likely that the approach presented here would also prove useful for that kind of problem.

8. Appendix: porosity corrections

If the value of internal porosity for all particles, n_{int}, is constant, intragranular porosity can be expressed as:

$$n^{\text{intra}} = \frac{\sum n_{\text{int}} V_T^p}{V_T} = n_{\text{int}} \frac{\sum V_T^p}{V_T} = n_{\text{int}} \left(1 - n^{\text{inter}}\right) \tag{23}$$

from this and the fact that $n = n^{inter} + n^{intra}$ follows

$$n = 1 - \left(1 - n^{\text{inter}}\right)\left(1 - n_{\text{int}}\right) \tag{24}$$

If internal porosity is variable, but a unique value of internal porosity $\overline{n}_{\text{int}}$ is assumed, intragranular porosity is only approximately computed. The difference between the exact value and the approximate value of intragranular porosity is given by a correction term, Δn

$$\overline{n}^{\text{intra}} = n^{\text{intra}} + \Delta n \tag{25}$$

The correction term is given by

$$\Delta n = \frac{1}{V_T}\left[\sum_p V_T^p n_{\text{int}}^p - \overline{n}_{\text{int}} \sum_p V_T^p\right] = n^{\text{intra}} - \overline{n}^{\text{intra}} \tag{26}$$

Only if $\overline{n}_{\text{int}}$ is selected as the volume-weighted particle porosity average, the correction term is 0. A relation analogous to (21) is still valid

$$\overline{n}^{\text{intra}} = \overline{n}_{\text{int}} \left(1 - n^{\text{inter}}\right) \tag{27}$$

Apparent and real porosities are related through the assumed value of internal particle porosity $\overline{n}_{\text{int}}$, since

$$n^* = 1 - \frac{\gamma_d}{\gamma_w \bar{G}_s} = \frac{(1-\bar{n}_{\text{int}})G_{s0} - (1-n)G_{s0}}{(1-\bar{n}_{\text{int}})G_{s0}} = \frac{(n-\bar{n}_{\text{int}})}{(1-\bar{n}_{\text{int}})} \qquad (28)$$

$$n = (1-\bar{n}_{\text{int}})n^* + \bar{n}_{\text{int}}$$

The question now is how to relate this apparent porosity n^* with the value of intergranular porosity n^{inter} that is requested to build a DEM model. We have

$$\bar{n} - \Delta n = (1-\bar{n}_{\text{int}})n^* + \bar{n}_{\text{int}} \qquad (29)$$

Combining the precedent expressions, and after some manipulation, the following relation is obtained

$$n^{\text{inter}} = n^* + \frac{\Delta n}{(1-\bar{n}_{\text{int}})} \qquad (30)$$

9. ACKNOWLEDGEMENTS

This work has been supported by the Ministry of Science and Innovation of Spain through the research grants BIA2011-27217 and BIA2014-59467-R

10. REFERENCES

Ahmed, S. M., Agaiby, S. W. & Abdel-Rahman, A. H. (2014). A unified CPT–SPT correlation for non-crushable and crushable cohesionless soils. *Ain Shams Engineering Journal* 5(1), pp. 63-73.

Almeida, M., Jamiolkowski, M. & Peterson, R., (1991). Preliminary result of CPT tests in calcareous Quiou sand. Proceedings of the International Symposium on Calibration Chamber Testing, Elsevier, New York, pp. 41-53.

Arroyo, M., Butlanska, J., Gens, A., Calvetti, F. & Jamiolkowski, M. (2011). Cone penetration tests in a virtual calibration chamber. *Géotechnique* 61 (6), pp. 525-531

Arroyo, M., Butlanska, J. & Gens, A. (2013). Effect of radial walls on CPT in DEM-based Virtual Calibration Chamber. Proceedings of the 3rd International Symposium on Computational Geomechanics (COMGEO III), Krakow, Poland

Ben-Nun, O. & Einav, I. (2010). The role of self-organization during confined comminution of granular materials. Philosophical Transactions of the Royal Society A: Mathematical, Physical and Engineering Sciences, Vol. 368, pp. 231-247.

Bolton, M. D., Nakata, Y. & Cheng, Y. P. (2008). Micro- and macro-mechanical behaviour of DEM crushable materials. *Géotechnique* 58(6), pp. 471-480.

Bruchmüller J., Van Wachem B.G.M., Gua, S. & Luo K.H. (2011). Modelling discrete fragmentation of brittle particles. *Powder Technology* 208, pp. 731-739

Brzesowsky, R. H., Spiers, C. J., Peach, C. J. & Hangx, S. J. T. (2011). Failure behavior of single sand grains: Theory versus experiment. *Journal of Geophysical Research: Solid Earth* (1978–2012), 116(B6).

Butlanska, J., Arroyo M. & A. Gens (2010a). Virtual Calibration Chamber CPT tests on Ticino sand. 2nd International Symposium on Cone Penetration Testing, CPT'10, Huntington Beach, California, pp. 217–224

Butlanska, J., Arroyo M. & A. Gens (2010b). Size effects on a virtual calibration chamber. 7th European Conference on Numerical Methods in Geotechnical Engineering, NUMGE 2010, Trondheim, pp. 225–230

699 Butlanska, J., Arroyo, M., Gens, A. & O'Sullivan, C. (2013). Multiscale analysis of CPT in a
700 virtual calibration chamber. *Canadian Geotechnical Journal* 51(1), pp. 51-66 [doi:
701 10.1139/cgj-2012-0476]
702 Butlanska, J., Arroyo M. & A. Gens (2014a). Steady state of solid-grain interfaces during
703 simulated CPT. *Studia Geotechnica et Mechanica* 35(4), pp. 13-22 [doi: 10.2478/sgem-
704 2013-0034]
705 Butlanska, J. Arroyo, M. & Gens, A. (2014b). Probing DEM specimen heterogeneity by
706 simulated CPT, International Symposium from Micro to Macro, Cambridge 2014,
707 Taylor & Francis, pp. 269 - 274
708 Casini, F., Viggiani, G. M. & Springman, S. M. (2013). Breakage of an artificial crushable
709 material under loading. *Granular matter* 15(5), pp. 661-673
710 Cheng, Y. P., Nakata, Y. & Bolton, M. D. (2003). Discrete el-ement simulation of
711 crushable soil. *Géotechnique* 53(7), pp. 633–641
712 Ciantia, M. O., Arroyo, M., Calvetti, F. & Gens, A. (2014a). Particle failure in DEM
713 models of crushable soil response. *Numerical Methods in Geotechnical Engineering*, pp. 345-
714 350 (ISBN: 978-1-138-00146-6)
715 Ciantia, M. O., Arroyo, M., Butlanska, J. & Gens, A. (2014b). DEM modelling of a
716 double-porosity crushable granular material. In K. Soga et al. (Ed.), Proc. of IS-Cambridge
717 2014 Int. Symposium on Geomechanics from Micro to Macro, p 269-274 *Taylor & Francis*
718 *Group, London, ISBN 978-1-138-02707-7*.
719 http://www.crcpress.com/product/isbn/9781138027077
720 Ciantia, M. O., Castellanza, R. & di Prisco, C. (2014c). Experimental study on the water-
721 induced weakening of calcarenites. *Rock Mechanics and Rock Engineering* 48, pp. 441–461.
722 Ciantia, M. O., Arroyo, M., Calvetti, F. & Gens, A. (2015). An approach to enhance
723 efficiency of DEM modelling of soils with crushable grains. *Géotechnique* 65(2), pp. 91–110.
724 Einav, I. (2007). Breakage mechanics—part I: theory. *J. Mech. Phys. Solids* 55, pp. 1274–
725 1297 [doi:10.1016/j.jmps.2006.11.003]
726 Esnault, V. P. B. & Roux, J. N. (2013). 3D numerical simula-tion study of quasistatic
727 grinding process on a model granu-lar material. *Mechanics of Materials* 66, pp. 88-109

728 Gabrieli, F., Cola, S. & Calvetti, F. (2009). Use of an up-scaled DEM model for analysing
729 the behaviour of a shallow foundation on a model slope. *Geomechanics and Geoengineering*:
730 *An International Journal* 4(2), pp. 109– 122
731 Itasca (2010). Particle flow code in three dimensions: Software manual. Minnesota, MN,
732 USA
733 Jamiolkowski, M., Lo Presti, D. C. F. & Manassero, M. (2003). Evaluation of relative
734 density and shear strength of sands from CPT and DMT. Soil Behavior and Soft Ground
735 Construction.
736 Jansen, U. & Stoyan, D. (2000). On the validity of the Weibull failure model for brittle
737 particles. *Granular Matter* 2(4), pp. 165-170.
738 Kuwajima, K., Hyodo, M. & Hyde, A. F. (2009). Pile bearing capacity factors and soil
739 crushabiity. *Journal of geotechnical and geoenvironmental engineering* 135(7), pp. 901-913.
740 Lin, J. & W. Wu (2012). Numerical study of miniature penetrometer in granular material
741 by discrete element method, *Philosophical Magazine* 92(28-30), pp. 3474–3482
742 Lobo-Guerrero, S. & Vallejo, L. E. (2005). DEM analysis of crushing around driven piles
743 in granular materials. *Géotechnique*, 55(8), pp. 617-623
744 Lunne, T., Robertson, P. K. & Powell, J. J. (1997). Cone penetration testing in
745 geotechnical practice. CRC Press
746 Marketos, G. & Bolton, M. D. (2009). Compaction bands simulated in discrete element
747 models. *J. Struct. Geol*. 31(5), pp. 479–490
748 Mayne, P.W. and Kulhawy, H. (1991). Calibration chamber database and boundary
749 effects corrections for CPT data. In Proceedings of the 1st International Symposium on
750 Calibration
751 Chamber Testing, pp. 1257–1264, Postdam, N.Y., 1991
752 McDowell, G.R. & de Bono, J. P. (2013). On the micro mechanics of one-dimensional
753 normal compression. *Géotechnique* 63(11), pp. 895-908
754 McDowell, G. R., Falagush, O. & Yu, H. S. (2012). A particle refinement method for
755 simulating DEM of cone penetration testing in granular materials. *Géotechnique Letters*
756 *2*(July-September), pp. 141-147

Meier, T., & Wehr, J. (2014). Influence of the calcite content of sands on the CPT-resistance. NUMGE 2014, 8th Conference on Numerical Methods in Geotechnical Engineering in Delft, The Netherlands, 18-20 June 2014

Minh, N. H. & Cheng, Y. P. (2013). A DEM investigation of the effect of particle-size distribution on one-dimensional compression, *Géotechnique* 63(1), pp. 44–53

Moss, R.E.S. (2014). A Critical State framework for seismic soil liquefaction triggering using CPT, 3rd International Symposium on Cone Penetration Testing, CPT14, May 12-14, 2014 - Las Vegas, Nevada, Paper 2#20

O'Sullivan, C. (2011). Particulate discrete element modelling. Taylor & Francis.

Parkin, A.K., & Lunne, T., (1982). Boundary effects in the laboratory calibration of a cone penetrometer for sand. Proceedings of the Second European Symposium on Penetration Testing, Amsterdam, 761-768

Quezada, J. C., Breul, P., Saussine, G. & Radjai, F. (2014). Penetration test in coarse granular material using Contact Dynamics Method. *Computers and Geotechnics* 55, pp. 248-253.

Robertson, P. K. (2009). Interpretation of cone penetration tests-a unified approach. *Canadian Geotechnical Journal* 46(11), pp. 1337-1355

Russell, A. R. & Muir Wood, D. (2009). Point load tests and strength measurments for brittle spheres. *International Journal of Rock Mechanics And Mining Sciences* 46, pp. 272–280

Russell, A. R., Muir Wood, D. & Kikumoto, M. (2009). Crushing of particles in idealised granular assemblies. *J. Mech. Phys. Solids* 57(8), pp. 1293–1313

Schnaid, F. (2009). In situ testing in geomechanics: the main tests. CRC Press.

Ting, J. M., Corkum, B. T., Kauffman, C. R. & Greco, C. (1989). Discrete numerical model for soil mechanics. *Journal of Geotechnical Engineering* 115(3), pp. 379-398

Tran, Q.A., Chevalier B. & Breul, P. (2014). A numerical study of the penetration test at constant rod velocity, Computer Methods and Recent Advances in Geomechanics – Oka, Murakami, Uzuoka & Kimoto (Eds.), Taylor & Francis Group 193-198

Wehr, W., (2005). Influence of the carbonate content of sand on vibro-compaction. Proceedings of the 6th International Conference on Ground Improvement Techniques, Coimbra, Portugal, pp. 625-632.

788 Weibull, W. (1951). A statistical distribution function of wide applicability. *Journal of*
789 *Applied Mechanics* 18, pp. 293-297
790 Wesley L. D. (2007). Geotecnical characteristics of a pumice sand. Characterisation and
791 Engieering properties of Natural Soils – Tan, Phoon, Hight & Leroueil (eds). ISBN 978-0-
792 415-42691-6
793 Wesley, L. D. (2001). Determination of specific gravity and void ratio of pumice
794 materials. *ASTM Geotechnical Testing Journal* 24(4), pp. 418-422.
795 Zhang, C., Nguyen, G.D., & Einav, I. (2013). The end-bearing capacity of piles penetrating
796 into crushable soils, *Géotechnique* 63 (5), pp. 341: 354
797 Zhao, Z. (2013). Gouge particle evolution in a rock fracture undergoing shear: a microscopic
798 DEM study. *Rock Mechanics and Rock Engineering* 46(6), pp. 1461-1479
799 Zhao, Z. & Song, E-x. (2015). Particle mechanics modeling of creep behavior of rockfill
800 materials under dry and wet conditions. *Computers and Geotechnics* 68, pp. 137-146
801

11. Tables

Table 1 Specimen tests: initial states. Inferred values in cursive

Case	*Test ID*	n^*	γ_d *(kg/m³)*	*n*	n^{inter}	n^{intra}
Experiment	"Dense"	0.55	*805*	*0.69*	*0.33*	*0.37*
Experiment	"Loose"	0.59	*722*	*0.72*	*0.37*	*0.35*
DEM	"Dense"	0.53	740	0.72	0.33	0.38
DEM	"Loose"	0.59	665	0.74	0.39	0.35

Table 2 Calibrated model parameters for pumice sand

ϕ **[rad]**	***G*** ***[kPa]***	ν ***[-]***	$\sigma_{lim,0}$ ***[kPa]***	***var*** ***[-]***	***m*** ***[-]***	d_0 ***[mm]***
0.4	3.33×10^5	0.3	1.16×10^5	0.5	5	2

Table 3 Comparative geometrical characteristics of experimental and simulated CC

Variable (unit)	**Symbol**	**Experiment**	**DEM-base**	**DEM-large**
Chamber diameter (mm)	D_C	760	760	760
Cone diameter (mm)	d_c	36	72.1	35.6
Chamber height (mm)	H	910	900	760
Particle mean size (mm)	D_{50}	1	22	15
Chamber/cone diameter ratio	$(D_C/d_c) = R_d$	21	10.5	21
Cone /particle ratio	$(d_c/ D_{50}) = n_p$	36	3.3	2.4
Friction sleeve height (mm)	h_s	133	133	133
Number of particles at 5 kPa	-	-	55385	203000

Table 4 CC initial states. Inferred values in cursive

			Experiment			**Simulation**		
Test ID	σ_{z0} *(kPa)*	σ_{h0} *(kPa)*	γ_d *(kg/m³)*	***n*** *(-)*	n^{inter} *(-)*	γ_d *(kg/m³)*	***n*** *(-)*	n^{inter} *(-)*
Dense 50	50	25	696	*0.73*	*0.39*	740	0.72	0.33
Dense 100	100	40	697	*0.73*	*0.39*	740	0.72	0.33
Dense 200	200	72	720	*0.72*	*0.37*	740	0.72	0.33
Loose 50	50	28	621	*0.76*	*0.43*	665	0.74	0.39
Loose 100	100	49	629	*0.76*	*0.42*	665	0.74	0.39
Loose 200	200	76	624	*0.76*	*0.43*	665	0.74	0.39

812 **Table 5 Parameters for the penetration curve adjusted to each simulated CPT**

	Crush			No-Crush		
Test ID	a	b	R^2	a	b	R^2
Dense 50	1.29	35.6	0.14	3.06	35.5	0.27
Dense 100	1.69	39.5	0.15	5.03	19.5	0.54
Dense 200	2.00	39.6	0.15	7.65	11.8	0.56
Loose 50	1.15	5.0	0.65	1.32	7.3	0.60
Loose 100	1.36	11.0	0.54	2.29	7.0	0.79
Loose 200	2.20	9.3	0.55	3.89	8.9	0.65

813

814

815

816 **Table 6 Crushing events during different test phases**

Density	**Vertical Stress**	**Phase**	**Crushing events in phase / initial particle number**	**Crushing events in phase / phase initial particle number**
Dense	50	compression	1.7%	1.7%
Dense	100	compression	2.4%	2.4%
Dense	200	compression	3.3%	3.5%
Dense	50	CPT	1.6%	2.2%
Dense	100	CPT	1.4%	2.1%
Dense	200	CPT	1.1%	1.7%
Loose	50	compression	1.8%	2.0%
Loose	100	compression	2.5%	3.0%
Loose	200	compression	3.5%	4.8%
Loose	50	CPT	1.0%	1.5%
Loose	100	CPT	1.1%	1.7%
Loose	200	CPT	1.4%	2.0%

817

818

819

12. List of symbols

ε_z is vertical deformation

ε_{vol} is volumetric deformation

σ_c is compressive strength

σ_t is tensile strength

$\sigma_c(d)$ is compressive strength as function of particle diameter

$\sigma_c(d = 2mm)$ is compressive strength for a 2mm diameter particle

$\sigma_t(d)$ is tensile strength as function of particle diameter

$\sigma_t(d = 2mm)$ is tensile strength for a 2mm diameter particle

ν is the Poisson's ratio

v_1 and v_2 are the Poisson ratio of the contacting spheres

θ_0 is a solid angle 'seen' from the center of the particle

ϕ is the interparticle friction angle

$\sigma_{\lim}$ is the limit strength

$\sigma_{\lim,0}$ is the mean limit strength

σ_{z0} is the chamber's vertical confinement stress

σ_{h0} is the chamber's horizontal initial confinement stress

σ_z is the vertical stress

σ is the CF standard deviation

μ is the CF ensemble average

γ_d is the dry unit weight

γ_w is the unit weight of water

A is a fitting parameter

a is a fitting parameter

A_F is the contact area

847 B is a fitting parameter
848 b is a fitting parameter
849 CC is calibration chamber
850 CF is contact force
851 d is the particle diameter
852 d_0 is the reference diameter (chosen as 2 mm)
853 d_{limit} is the comminution limit
854 d_1 and d_2 are the diameters of the two spheres in contact
855 d_c cone diameter
856 D_c chamber diameter
857 D_{50} is the mean particle diameter
858 E_1 and E_2 are the Young modulus of the contacting spheres
859 f_1 is the strength correction factor 1
860 f_2 is the strength correction factor 2
861 F is the magnitude of the normal contact force
862 F_n is the normal and shear contact force component
863 F_t is the shear contact force component
864 $F_{\lim}$ is the magnitude of the limit normal contact force
865 G_{s0} specific gravity of quartz
866 $G_s(d)$ is the apparent specific gravity of a particle with diameter d
867 $\bar{G}_s$ is the constant apparent specific gravity
868 G is the shear modulus
869 GSD is the grain size distribution
870 H is the chamber height
871 h_s is the friction sleeve height
872 h_p is the penetration depth
873 k_N normal contact stiffness
874 k_S tangential contact stiffness
875 m is a material parameter
876 N is the scaling factor

877 n is the total porosity

878 n_{int} is the internal porosity

879 n_{int}^{p} is the internal porosity of particle *p*

880 n^{inter} is the total volume fraction not occupied by particles

881 n^{intra} is the total volume fraction occupied by internal voids

882 $\overline{n}_{\text{int}}$ is the constant internal porosity

883 $\overline{n}^{\text{int}ra}$ is the approximate value of n^{intra}

884 n^{*} is the apparent porosity

885 n_p is the cone/mean particle diameter ratio

886 q_c is the cone tip resistance

887 r_H is the radius of the contact area

888 R_d is the Chamber/cone diameter ratio

889 r_1 and r_2 are the radius of the contacting spheres

890 r is the sphere radius

891 U is the sphere overlap

892 *var* coefficient of variation

893 V_V^p is the volume of the voids within particle *p*

894 V_T^p is the total volume of particle *p*

895 V_S^p is the solid volume for particle *p*

896 V_T is the total volume

897 V_s total solid volume for a collection of *p* particles

898

899